Exploring the importance of authigenic clay formation in the global Li cycle

Elizabeth Andrews[1,2,*], Philip A. E. Pogge von Strandmann[3], and Matthew S. Fantle[1]

1 – Dept. of Geosciences, The Pennsylvania State University, University Park, PA 16802

2 – Hydrologic Science and Engineering, Dept. of Geology and Geological Engineering, Colorado School of Mines, Golden, CO 80401

3 – London Geochemistry and Isotope Centre (LOGIC), Institute of Earth and Planetary Sciences, University College London and Birkbeck, University of London, Gower Place, London, WC1E 6BS, UK

* Corresponding author: eandrews1@mines.edu, Tel: +1 484-767-0593

Keywords: global Li cycle; Li isotopes; reactive transport modeling; clay authigenesis; geochemical proxies; carbonate-rich marine sediments

Abstract

Lithium isotopic (δ^7Li) and elemental concentrations in pore fluids and carbonates from IODP Site U1338 Hole A (eastern equatorial Pacific Ocean) suggest that clay authigenesis (i.e., *in situ* precipitation) is a significant sink for Li in carbonate-rich sedimentary sections. Systematic variations in pore fluid δ^7Li with depth in the section suggest that clay authigenesis can (i) strongly decrease pore fluid Li concentrations with depth and (ii) fractionate Li isotopically to a considerable degree ($\Delta \sim 5$ to 21‰ relative to seawater). We hypothesize that clay authigenesis in carbonate-rich sections occurs in the presence of reactive biogenic silica, and reactive transport modeling supports the contention that the pore fluid δ^7Li depth profile at Site U1338 is best explained by faster authigenesis at depth. The significance of clay authigenesis in carbonate-rich sediments is two-fold: if global in scale, (i) it can generate sizeable output fluxes in the global Li cycle, and (ii) the evolution of the sedimentary system over time can markedly impact the isotopic composition of the global Li output flux. We compile ODP and IODP pore fluid Li data from 267 sites; of these, 207 have Li pore fluid concentration gradients in the upper 50-100 meters that indicate the sites as diffusive sinks of Li. We then estimate that clay authigenesis in carbonate-rich sediments could reasonably generate a Li output flux on the order of $\sim 1.2 \cdot 10^{10}$ moles/year, which is comparable to the gross input fluxes in the modern Li cycle. A series of reactive transport simulations illustrate how clay authigenesis might impact the isotopic composition of the output flux of Li from the global ocean. The suggestion is that applying a constant fractionation factor from the global ocean over time is likely incorrect, and that secular changes in the δ^7Li of the output flux will be driven by rates of authigenesis, burial rates, and the depth extent of authigenesis in the sedimentary section. Utilizing a time-dependent, depositional diagenetic model, the δ^7Li values of bulk carbonate are shown to be a consequence not of recrystallization alone, but recrystallization in the presence of clay authigenesis. Further, our model results are used to illustrate how carbonate δ^7Li may be used to constrain the temporal evolution of clay authigenesis in the sedimentary section. Ultimately, this work suggests that the Li isotopic composition of bulk carbonates can be altered diagenetically. However, such alteration is not a detriment, but provides useful information on those diagenetic processes in the sedimentary column that impact the global Li cycle. Thus, Li isotopes in bulk carbonates have the potential to elucidate diagenetic controls on the global Li cycle over long time scales.

1. Introduction

The desire to reconstruct carbon cycling and climate variability over geologic time scales has spurred development of novel isotopic proxies that can constrain processes within the carbon cycle, such as silicate weathering, that act as feedbacks on atmospheric CO_2 concentrations over geologic time scales. Lithium (Li) isotopes have been proposed as proxies for present and past continental silicate weathering (Millot et al., 2010; Pogge von Strandmann et al., 2013; Dellinger et al., 2014; Dellinger et al., 2017), and, accordingly, have been measured in both carbonate and

siliciclastic sediments in order to quantify the intensity of continental weathering over geologic time scales (e.g., Misra and Froelich, 2012; Pogge von Strandmann et al., 2017). The Li isotopic composition of seawater is impacted by silicate rock weathering but is much less sensitive to carbonate rock weathering (Kisakurek et al., 2005), which is the basis for the proposal that Li isotopes are ideal tools for reconstructing the secular evolution of silicate weathering processes. One approach that has been used quite successfully is to utilize carbonate minerals (such as foraminiferal tests) as proxy archives to reconstruct the δ^7Li of seawater, and then interpret this signal in terms of the silicate weathering input to the ocean over geologic time scales (Misra and Froelich, 2012; Pogge von Strandmann et al., 2013; Lechler et al., 2015). Carbonate is a reasonable archive because while the Li isotopic composition of foraminiferal tests can be species specific, they appear to closely reflect the δ^7Li of the water in which they grew (Hall et al., 2005; Hathorne and James, 2006; Vigier et al., 2007; Dellinger et al., 2018). It is also worth noting that one assumption that is made when interpreting the putative seawater δ^7Li record is that secular variability in seawater δ^7Li is driven almost entirely by variations in the riverine input flux.

Before reconstructing secular trends in silicate weathering using any proxy archive, be it siliciclastic or carbonate, it is crucial to consider the effect of post-depositional (or post-formational) alteration of the archive (i.e., diagenesis). Bulk carbonates have been shown to react and recrystallize relatively rapidly (Fantle and DePaolo, 2007; Fantle, 2015; Gorski and Fantle, 2017; Huber et al., 2017), impacting strontium, oxygen, and magnesium isotope compositions and Mg/Ca ratios (Richter and DePaolo, 1987; Schrag et al., 1992; Fantle and DePaolo, 2006; Chanda and Fantle, 2017). In contrast to elements such as Ca and Sr, and similar to Mg, Li has a low concentration in carbonates (1-2 ppm; Hoefs and Sywall, 1997; Burton and Vigier, 2012)

compared to its concentration in siliciclastics (50-500 ppm; Hein et al., 1979; Zhang et al., 1998). Likewise, siliciclastic sediments have also been inferred to be reactive: biogenic silica has been proposed to react in the sedimentary column to form authigenic clays (Michalopoulos and Aller, 1995; Michalopoulos et al., 2000; Michalopoulos and Aller, 2004), while amorphous silica has been shown to react even over short, laboratory time scales (Geilert et al., 2014; Roerdink et al., 2015; Fernandez et al., 2019).

Despite the clear evidence for mineral reaction in the sedimentary column, there has been a limited amount of work on the impact of diagenesis on the Li isotopic composition of proxy archives (You et al., 2003; Ullmann et al., 2013; Dellinger et al., 2020). While carbonate recrystallization has been the focus of Li-based diagenetic studies to date, authigenic clay formation, in particular, has the potential to impact carbonate archives in a range of ways. First, carbonate-hosted Li is susceptible to contamination by relatively small amounts of siliciclastic material (e.g., authigenic clays) that may be intimately associated with carbonate minerals and/or fossils. Second, authigenic clay formation at depths in the sedimentary column that are out of diffusive communication with the overlying seawater reservoir can shift pore fluid δ^7Li to markedly higher values than seawater, which increases the isotopic leverage to alter via recrystallization (Zhang et al., 1998; Pistiner and Henderson, 2003; Chan et al., 2006; Vigier et al., 2008; Wimpenny et al., 2015; Hindshaw et al., 2019; Pogge von Strandmann et al., 2019a; Fantle et al., 2020). It remains to be seen, however, whether or not clay authigenesis is important in carbonate-rich sediments.

If clay authigenesis is significant in carbonate-rich sediments, then there is potential for this diagenetic process to impact the global Li cycle to a considerable extent. While the question of whether marine sediments are marine Li sources or sinks has been debated for decades

(Stoffyn-Egli and Mackenzie, 1984; Huh et al., 1998; Misra and Froelich, 2012), the focus has mainly been on siliciclastic, and not carbonate-rich, sections. Prevailing wisdom holds that the balance between dissolution and precipitation of Li-containing silicates in marine sedimentary systems dictates whether a given sedimentary section is a Li source or sink (Stoffyn-Egli and Mackenzie, 1984). Because biogenic carbonates have very low Li concentrations, there is considerable potential to develop strong diffusive gradients, and thus large output fluxes, in carbonate-rich sections. Further, there is potential for such output fluxes to evolve elementally and isotopically over time. Ultimately, then, identifying the spatial extent of authigenesis in the sedimentary column, quantifying its impact on the global Li cycle, and elucidating its evolution over time is critical, as this sink plays an important role in balancing hydrothermal, riverine, and subduction reflux inputs over geologic time scales (Hathorne and James, 2006; Misra and Froelich, 2012).

If we are to use Li isotopes in carbonate-rich sediments to peer into the past confidently and unambiguously, we must understand the systematics of authigenesis. Amongst the questions that must be addressed in order to build that confidence are:

(1) Does authigenic clay formation impact the Li isotopic composition of carbonate proxy archives?
(2) Does carbonate recrystallization incorporate the signal of pore fluid whose chemistry is impacted by clay authigenesis?
(3) Are sizeable fluxes in the global Li cycle associated with carbonate-rich sites? If so, what is the isotopic fractionation associated with such fluxes and does this evolve over time?

With these questions in mind, the objective of the current study is to investigate the impact of diagenesis on the Li isotopic composition of bulk carbonates in a carbonate-rich section in the eastern equatorial Pacific (IODP Leg 321, Site U1338, Hole A; 2°30.469'N, 117°58.178'W). This

site was chosen because there is a significant pore fluid Li concentration gradient in the sedimentary column that presumably represents the balance between diffusion of Li into the sediment and removal from pore fluids by reaction in the sedimentary column. We analyzed the elemental and isotopic composition of Li in a suite of pore fluids from Site U1338, as well as sequentially leached bulk carbonates. Selected sediments were imaged using scanning electron microscopy (SEM) and energy dispersive spectroscopy (EDS) to determine qualitative spatial trends in the chemistry of particles sampled from the sedimentary column, while mineralogy was constrained by powder X-ray diffraction (XRD). Multicomponent reactive transport modeling was conducted in order to constrain the balance between clay authigenesis and biogenic silica dissolution at Site U1338; a diffusion experiment was also performed to help constrain the fractionation factor associated with diffusion, given the dearth of existing constraints. The constraints provided by the modeling are then utilized to discuss the global relevance of clay authigenesis in carbonate-rich sections.

Ultimately, our analysis suggests that authigenic clay formation (i) occurs in carbonate-rich sections, (ii) controls the Li isotopic composition of pore fluids, and (iii) has the potential to impact the Li isotopic composition of bulk carbonates. Clay authigenesis could account for as much as a $\sim 1.2 \cdot 10^{10}$ mol Li/ year output flux in the global Li cycle, which is similar in magnitude to the marine authigenic clay flux constrained by Hathorne and James (2006) and Misra and Froehlich (2012). Interestingly, this flux has the potential to vary temporally in both mass flux and isotopic composition, which could help explain the evolution of seawater δ^7Li over million-year time scales.

2. Site Description

Site U1338 was drilled in 2009 during IODP Expedition 320/321, the goal of which was to collect an age transect of Cenozoic sediments deposited at the paleo-position of the equator across the eastern equatorial Pacific Ocean (see Figure 1 for location of drill sites). The oldest site (U1331) sits on 53 Ma basaltic basement, while the youngest site (Site U1338) sits conformably on 18 Ma basement. Four holes were drilled at Site U1338 (A, B, C, and D); in this study, we focus on Hole A. The water depth at Site U1338, Hole A is ~4205 meters and drilling penetrated 410 meters in the sedimentary column, which is comprised primarily of nannofossil ooze, with varying amounts of foraminifers and biogenic silica (Palïke et al., 2010b).

Stratigraphically, the sediment column contains three distinct lithostratigraphic units (Fig. 1b). Unit I (from 0 to 50 meters below seafloor, mbsf) consists of Pleistocene to mid-Pliocene sediment, which is primarily white, brown, and gray nannofossil ooze containing variable amounts of diatoms and radiolaria (Palïke et al., 2010b). The second unit, Unit II, encompasses the upper Miocene to the mid-Pliocene between 50.35 and 243.94 mbsf, and consists of light green and light gray nannofossil ooze with dark, diatom-rich intervals. Mottling/color changes in this unit likely represent variations in redox state (Palïke et al., 2010b). The final sedimentary unit, Unit III, is lower to upper Miocene in age and spans 243.94 to 408.37 mbsf. Unit III consists of white, pale yellow, light greenish gray, and very pale brown nannofossil oozes and chalks. In Unit III, there are darker green and gray intervals that contain more siliceous microfossils. Unit III conformably overlies the 18 Ma basaltic basement (Palïke et al., 2010b). On the revised method composite depth (rmcd) scale, which allows for comparisons between sites, the unit intervals are 0 to 55.91 rmcd for Unit 1, 55.91 to 271.72 rmcd for Unit II, and 271.72 to 453.43 rmcd for Unit III (the rmcd scale will be used throughout this paper).

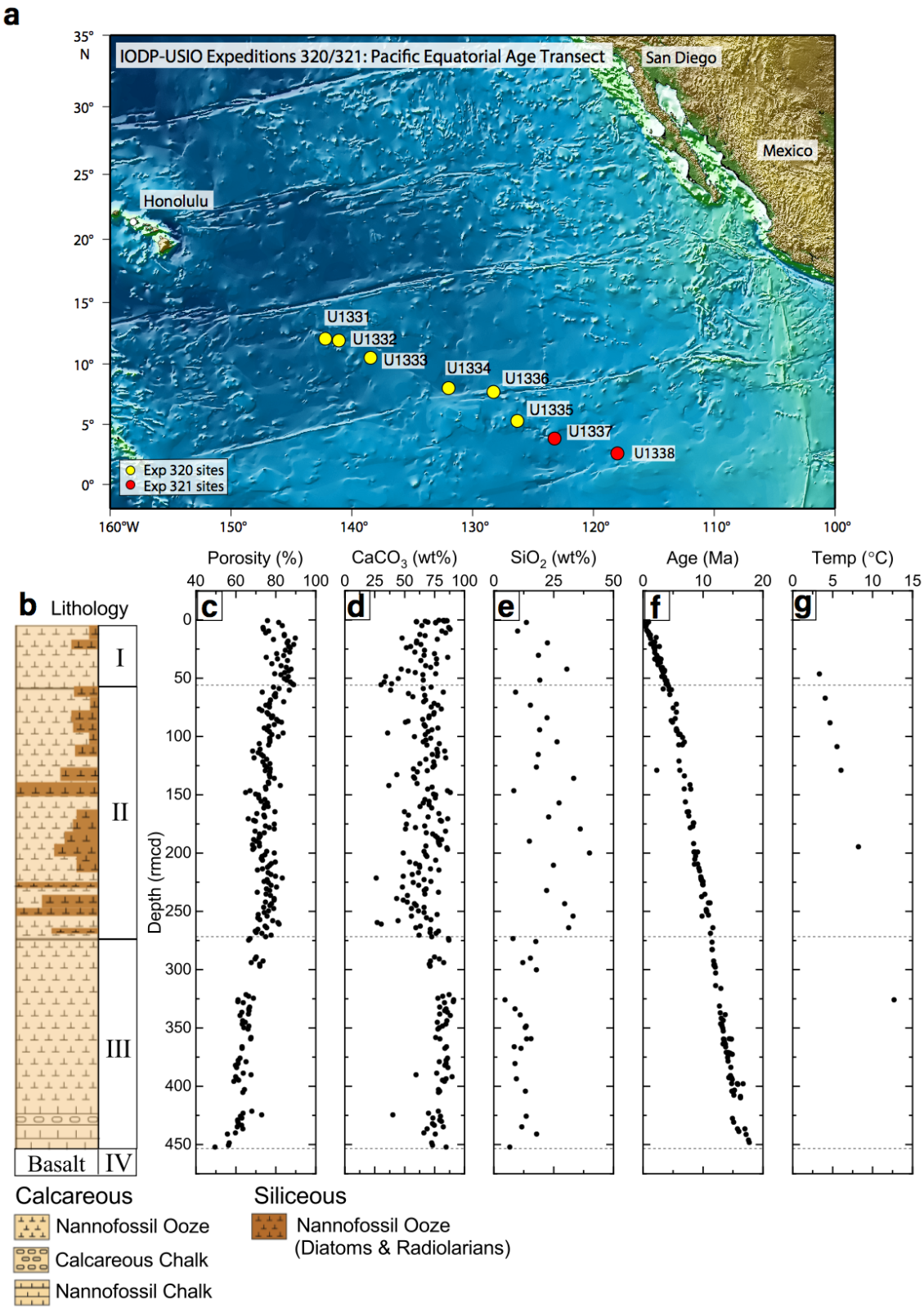

Figure 1. (a) Location of IODP Expedition 320/321 drill sites. Map courtesy of IODP-JRSO. (b) Stratigraphic column and lithologic unit, (c) porosity of the section, (d) weight percent

158 $CaCO_3$ in sediment, (e) weight percent SiO_2 in sediment, (f) age-depth profile for the section, and
159 (g) temperature-depth profile for Site U1338A. Data from Palïke et al. (2010b)
160

161 Porosity at Site U1338, Hole A decreases with depth, from ~80% at the sediment-water interface
162 to ~50% near the sediment-basement interface (Fig. 1c). Carbonate content varies between ~26
163 and ~91 wt. %, while SiO_2 content ranges from ~5 to 53 wt. % (Fig. 1d and 1e). In the upper 250
164 meters, the $CaCO_3$ content is high but variable, ranging from 26 to 88 wt. %, while the SiO_2
165 content ranges between ~10 and 40 wt. % (Palïke et al., 2010b). Below 250 meters, the
166 variability in the solid phase $CaCO_3$ content decreases, ranging between 66 and 91 wt. %; the
167 solid phase SiO_2 content in this interval varies between 10 and 20 wt. %. Several measurements
168 of temperature were made during drilling: at the sediment-water interface, the temperature was
169 ~1.6˚C, and increased with depth from 3.3˚C at ~41 rmcd to 12.7˚C at ~325 rmcd (Fig. 1g)
170 (Palïke et al., 2010b).

171 Major and trace elements were analyzed in the squeeze-cake pore fluids during the cruise
172 by inductively-coupled plasma atomic emission spectroscopy (ICP-AES) (Palïke et al., 2010a).
173 The most notable geochemical trend with depth is the pore fluid Li concentration, which
174 decreases strongly with depth from the seawater value (26 μM) to a minimum of ~2 μM at 250
175 meters, before increasing again to seawater concentration (26 μM) near the sediment-basement
176 interface (Fig. 2a). The increase in Li concentration at the sediment-basement interface has been
177 inferred to be the result of advective seawater flow through the basement (Palïke et al., 2010b).
178 The pore fluid Sr concentration profile is also significant, increasing with depth to a maximum of
179 ~400 μM at ~240 meters before decreasing with depth to seawater values (~90 μM) (Fig. 2b).
180 The increase in Sr concentration with depth likely represents dissolution and/or recrystallization

of biogenic carbonate (Palïke et al., 2010b). Estimates of recrystallization extent are ~20% at 18 Ma (Voigt et al., 2015).

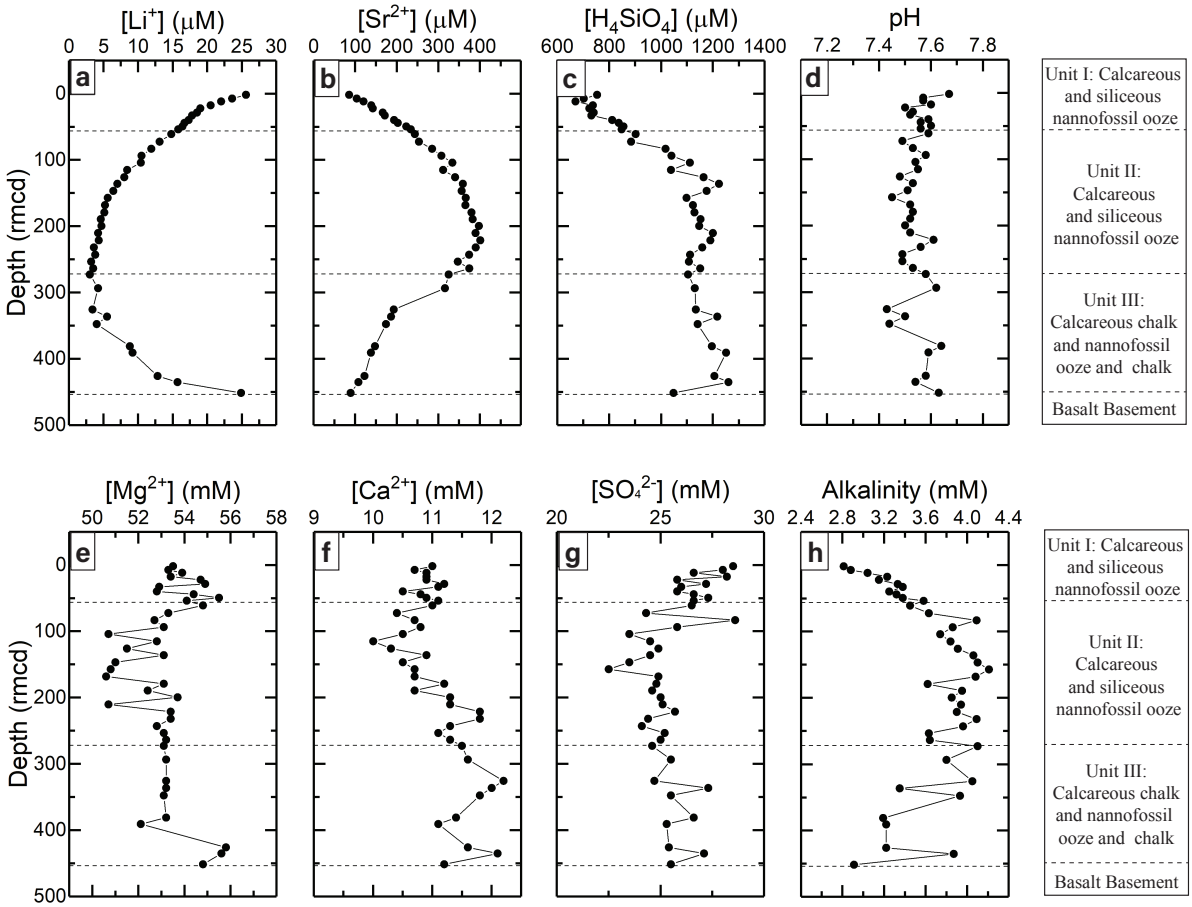

Figure 2. Pore fluid chemistry of Site U1338A. (a) Li concentration, (b) Sr concentration, (c) H_4SiO_4 concentration, (d) pH, (e) Mg concentration, (f) Ca concentration, (g) sulfate concentration, and (h) alkalinity. Simple unit descriptions and boundaries are added for clarity. Data from Palïke et al., (2010b).

Pore fluid silicic acid concentrations increase linearly with depth and stabilize at ~1200 μM until just above the sediment-basement interface. It has been suggested that the dissolution of biogenic silica causes the increase in silicic acid concentrations (Palïke et al., 2010b) (Fig. 2c). The alkalinity depth trend is similar to that of silicic acid; alkalinity increases from 2.7 mM at the sediment-water interface to 4.2 at ~150 meters. Below 150 rmcd, the alkalinity becomes more

194 variable, but the general trend is a decrease with depth towards 2.8 mM at the sediment-
195 basement interface (Fig. 2h). The pH ranges from 7.4 to 7.7, decreasing slightly over the upper
196 250 meters and increasing to ~7.6 at the sediment-basement interface (Fig. 2d). Dissolved Mg,
197 Ca, and sulfate decrease slightly in the uppermost 200 meters of the section. Below 200 rmcd,
198 the Mg and SO_4^{2-} concentrations remain relatively constant while Ca concentrations increase
199 slightly (Fig. 2e,f,g).

200

201 3. **Methods**

202 *3.1 Analytical Techniques*

203 The pore fluids were collected through whole-round squeezing completed on the Joides
204 Resolution. Upon arrival at Penn State, the pore fluids were filtered through an acid-washed 0.2
205 µm PVDF (polyvinyldiene fluoride) syringe filter. Samples were then digested using perchloric
206 acid ($HClO_4$) and hydrofluoric acid (HF) to remove organics and dissolved silica. A small
207 aliquot of each sample (pre-digestion) was analyzed on ICP-AES and ICP-MS (inductively
208 coupled plasma atomic emission spectroscopy and mass spectrometry) to determine the
209 concentration of major and trace elements, including Li, in the pore fluid. The total charge
210 equivalent of the sample was calculated along with the Li concentration to determine the amount
211 of sample to be loaded on an ion exchange column for separation of Li from the matrix.

212 To obtain a sufficient amount of Li for isotopic analysis, 1 g of sediment sample was
213 sequentially extracted following a slightly modified Tessier extraction designed to dissolve bulk
214 carbonates for trace metal analysis (Apitz, 1991; Delaney and Linn, 1993). Bulk sediments were
215 first treated with 50 mL of 1 N ammonium hydroxide (NH_4OH) to release Li (and other cations)
216 bound to exchange sites. The samples were subsequently rinsed with 18.2 MΩ deionized water

(MQ water) buffered to pH 10 with NH_4OH. Carbonates were then dissolved in 1 N acetic acid for 5 hours and centrifuged; the supernatant was decanted and saved. This acetic acid leach was not buffered with sodium acetate as described in the original extraction method to avoid adding additional cations (such as Na^+) to the solution. The carbonate extraction was filtered through a 0.2 μm PVDF filter and analyzed for Li using a X-Series II quadrupole ICP-MS in the Laboratory for Isotopes and Metals in the environment (LIME). The residual solid (silicates and biogenic silica) was then digested using a mixture of concentrated HNO_3, HCl, $HClO_4$, and HF. Upon complete dissolution of the solid, the solution was then analyzed for cations by Perkin-Elmer 5300 Optima 5300DV ICP-AES and for Li by ICP-MS. The errors associated with concentration measurements are approximately 2%, as determined by repeated analysis of in-house laboratory standards.

The mineralogy of the non-carbonate fraction of the sediment was determined by powder X-ray diffraction. Prior to analysis, the samples were treated with 1 N acetic acid to remove carbonate so that the trace phases in the sediment could be identified. Samples were then rinsed with MQ water and wet sieved. The < 63 μm size fraction was dried at 30˚C and analyzed. A PANalyical X'Pert Pro MPD X-ray Diffractometer with a copper tube and an X-ray wavelength (K_α) of 1.541874 Å was used for the analysis. Scanning occurred for a total of 17 minutes and ranged from 5˚ to 70˚ 2θ.

Electron microscope images of the samples were taken using a FEI Nova NanoSEM 630 Scanning Electron Microscope at the Materials Research Institute (MRI) at Penn State. Samples were wet sieved with water, allowed to air dry, and the >63 μm fraction was attached by carbon tape to an aluminum stub. The stubs were coated with 5 nm of iridium to minimize sample charging and permit qualitative elemental analysis using standard-less energy dispersive

spectroscopy (EDS). Scanning electron images were typically taken at a working distance of 3 mm, a voltage of 5 to 10 keV, and a spot size of 3.0 nm. EDS data, which were used to assess the chemical composition of the sediments, were collected at 10 keV and a spot size of ~6.0 nm. Scans were collected for 2 minutes and the data analyzed, and elemental maps generated, using Aztec EDS software.

Prior to isotopic analysis, Li in pore fluids and the residual fraction of the sediments was purified chromatographically using AG-50Wx12 200-400 mesh resin in polypropylene Bio-Rad columns. The bed volume of the column is 2 mL and the column has an 8 mL reservoir volume. The resin was pre-washed in batches with 4 N HCl and 4 N HNO_3. The columns were loaded to 2 mL, which was approximately 8 cm in height. The resin was washed again in column with 4 N HCl and 4 N HNO_3 and then conditioned with 0.2 N HCl. Samples were loaded onto the column in ~0.2 mL of 0.2 N HCl. Elution of Li was carried out with ~30 mL of 0.2 N HCl, then the matrix was cleaned out of the column with 4 N HCl. The procedural blank was less than 0.8 ng of Li. No Li was detected in the procedural blank on the ICP-MS where the detection limit was 0.1 ng/g in an 8 mL sample. The Li cut and the post cut were both analyzed by ICP-MS to calculate column yields (ranged between 98 and 104%), as incomplete recovery can cause significant fractionation (Tomascak et al., 2016). To ensure good yields, the total mass loaded onto the column was limited to <7.5% of the cation exchange capacity (c.e.c.) of the column. In samples with low Li:Na ratios, the sample was purified on multiple columns in parallel in order to maintain this cutoff. Samples were dried down and resuspended in 2% HNO_3 to ~30 ppb prior to analysis on the ThermoFisher Scientific Neptune Plus MC-ICP-MS in the Metal Isotope Laboratory (MIL) at Penn State.

Isotopic analysis was conducted on pore fluid and residual fraction samples and standards that had a Li concentration of ~30 ppb. Sample-standard bracketing was utilized, in which reagent blanks (BLK) were also measured (i.e., in the sequence: BLK-STD-BLK-SAMP-BLK-STD-BLK); the measured blank was corrected for by averaging the bracketing blank ratios and subtracting that value from the measured standard and sample values (see Eqn. S2 in Supplemental Information for details). The bracketing standard used was IRMM-016, which is isotopically similar to L-SVEC ($\Delta^7Li_{IRMM\text{-}016\text{-}LSVEC}$ = -0.2±0.3‰, Tomascak et al., 2016), and all delta values are reported relative to this standard. The notation for isotopic measurements is:

$$\delta^7Li = (({}^7Li/{}^6Li)_{sample} / ({}^7Li/{}^6Li)_{IRMM\text{-}016} - 1) \cdot 10^3 \quad [1]$$

where the standard ratio represents the average of the bracketing standard measured before and after the sample and blank. Repeated analysis of international standards were in agreement with literature values: analysis of IAPSO yielded $\delta^7Li = 31.2 \pm 0.9$ and analysis of BCR-1 yielded $\delta^7Li = 2.8 \pm 0.7$‰ (in agreement with Magna et al., 2004 and Rudnick et al., 2004). All reported errors are 1 standard deviation.

The carbonate and exchangeable fractions of the leaches were chromatographically separated and analyzed in the London Geochemistry and Isotope Centre (LOGIC). Sufficient leachate was evaporated to attain ~5ng of Li, and passed through a two-stage cation exchange column procedure (AG50W X-12), eluting with dilute HCl (Pogge von Strandmann et al., 2011). Column splits collected before and after the main elute, and analyzed for Li contents, show that for each sample >99.9% of the sample was collected for isotopic analysis.

Purified carbonate and exchangeable leach samples with a concentration of 5 ppb were analyzed on a Nu Plasma 3 MC-ICP-MS, using a sample-standard bracketing procedure relative

to IRMM-016. Each sample was measured three separate times during each analytical procedure, repeat measurements being separated by several hours (but during the same analytical session). We present the two standard deviation of these three repeats as the internal uncertainty on each sample. Subsequent to analysis, sample δ^7Li was renormalized to the LSVEC standard, as detailed in Pogge von Strandmann et al. (2019). The results of different international rock and solution standards analyzed by this method are detailed in Pogge von Strandmann et al., 2011, 2019. Seawater analyzed during these particular analytical runs yielded δ^7Li = 31.4 ± 0.2 and 31.2 ± 0.2‰.

3.2 Multicomponent Reactive Transport Modeling

Multicomponent reactive transport modeling was conducted using CrunchTope, a reactive transport code that incorporates isotopes (see Druhan and Maher, 2014; Steefel et al., 2014; Steefel et al., 2015 for governing equations and Supplemental Information for example of input file blocks detailing initial and boundary conditions, as well as transport parameters). Briefly, CrunchTope uses the advection dispersion equation to calculate transport; mineral dissolution and precipitation are governed by kinetic rate laws following Transition State Theory. Variability in the isotopic composition of model pore fluids can be generated by (i) differences in the rate constants for nuclide-specific precipitation reactions ($\alpha_{clay–fluid} \approx 0.986$-0.990; Pistiner and Henderson, 2003; Vigier et al., 2008), (ii) distinct stoichiometries of dissolving minerals (i.e., biogenic silica), and/or (iii) differences in the diffusion coefficients for $^6Li^+$(aq) and $^7Li^+$(aq) (see below). The objectives of the modeling were to estimate the rate of clay authigenesis that would explain the Li isotopic and elemental pore fluid data, predict the volume of secondary clays this process would produce, and to investigate various scenarios with

307 respect to reactivity within the sedimentary column. The model domain was a one-dimensional
308 column containing 460 nodes spaced at 1 m (i.e., representative of Site U1338). Dirichlet
309 conditions were set at the upper and lower boundaries of the domain, which permitted transport
310 fluxes across both boundaries. No lateral flow was allowed.

311 The measured sediment lithology at Site U1338 constrained the initial conditions
312 assumed in all Site U1338-specific reactive transport models. The initial model solid phase, for
313 instance, was constrained by the average geochemistry (e.g., $CaCO_3$ and SiO_2 weight percent,
314 porosity, etc.) of the previously described lithologic units (Units I and II are combined, while
315 Unit III is considered a separate zone). Initial pore fluid Li concentration and isotopic
316 composition is assumed to be the same as modern seawater (m_{Li^+} = 26 μM; δ^7Li = 31.5‰).
317 Model porosities are set to 0.75 for Units I and II and 0.63 for Unit III, reflecting the average
318 measured porosity of each unit. The temperature in the model was assumed to be a uniform
319 10˚C, unless otherwise noted; the temperature determined the diffusion coefficients defined in
320 the TRANSPORT block of the input file (see SI for details).

321 Burial can be applied in CrunchTope such that material is added to the top of the section,
322 though CrunchTope does not do compaction and thus maintains a constant sedimentary column
323 thickness. Therefore, if material is added at the top in a given time step, then material must be
324 removed at the bottom. This means that the entire section cannot be modeled using one burial
325 condition; if one is interested in the chemical evolution at the top of the section, burial can be
326 turned on. However, if one wants to simulate the evolution at the bottom boundary (i.e., the
327 sediment-basement interface), burial must be zero. In simulations in which burial is applied, a
328 sedimentation rate of ~23 m/Ma is utilized, which is the average sedimentation rate for the

329 section over the past ~20 Ma (Palïke et al., 2010b). In models in which only the last 10.6 Ma is
330 simulated, the burial rate is 23.7 m/Ma.

331 While the model framework permitted solute transport by advection, no advection
332 velocity was applied in the simulations performed given the lack of observational evidence for
333 advection in the sedimentary column. While it is certainly possible that advection occurs in this
334 section, advective fluxes in thick, fine-grained, low permeability carbonate sediments are
335 generally chemically undetectable (Spinelli et al., 2004). Thus we ignore advection; the primary
336 means by which solutes are transported in the fluid is therefore aqueous diffusion. Species-
337 specific diffusion coefficients are defined for all aqueous species at the temperature set for any
338 given simulation (see SI for details). The aqueous $^{6}Li^{+}$ and $^{7}Li^{+}$ species are assigned nuclide-
339 specific diffusion coefficients that differ, allowing for fractionation during diffusion. The
340 fractionation factor associated with diffusion ($D_{7_{Li}}/D_{6_{Li}}$= 0.99822) was determined
341 experimentally (see SI for details) and is similar to previously reported isotopic fractionation
342 factors associated with low-temperature diffusion (i.e., 0.99772 from Richter et al., 2006, and
343 0.991-1.0 from other low temperature studies (Verney-Carron et al., 2011)).

344

345

346

347 **4. Results**

348 *4.1 Lithium Isotopic Compositions ($\delta^{7}Li$) of Pore Fluids: Site U1338 Hole A*

349 The Li isotopic compositions of pore fluids ($\delta^{7}Li$) range between ~28‰ and ~52‰ (Fig.
350 3). Delta values are close to that of modern seawater at the top of the section (1.5 rmcd) and

increase systematically with depth to a maximum value of 51.8‰ at ~325 rmcd (Fig. 3). Below this maximum, δ^7Li values decrease towards seawater values at the lower sediment-basement interface (Fig. 3). The maximum pore fluid δ^7Li value occurs in Unit III, and the most significant rate of change (i.e., $d\delta^7Li/dz$) occurs close to the boundary between Unit II and Unit III.

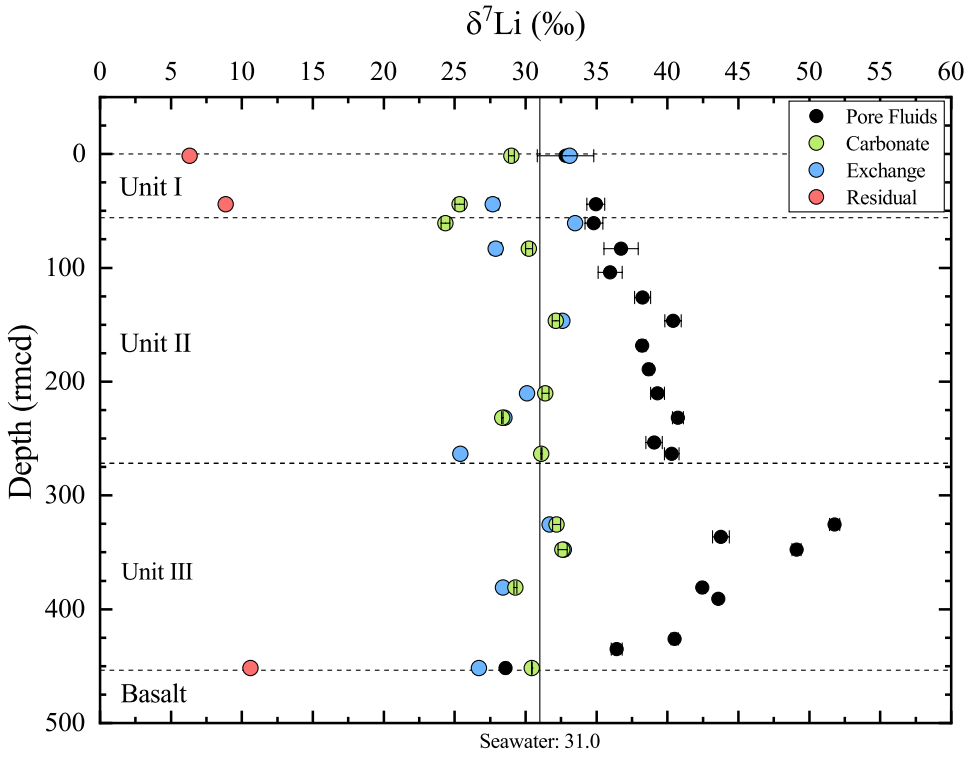

Figure 3. Lithium isotopic composition of pore fluids, exchangeable fraction, carbonate fraction and residual silicate fraction at Site U1338A. The error bars represent 1 standard deviation. The vertical line represents the isotopic composition of modern seawater and the horizontal lines represent unit boundaries.

4.2 Lithium Concentrations and Isotopic Compositions of Sequential Extractions: Site U1338 Hole A

Sequential extractions of the bulk solid were conducted to understand how Li is apportioned in the bulk sediment. The Li concentration depth profiles of both the exchangeable fraction and the acetic-soluble carbonate are similar to that of the pore fluid (Fig. 4). In order to

compare across the various fractions, all concentrations are expressed in mass of Li (ng) per cm^3 of porous medium (Table S5 in the supplement contains the mass of Li per g sediment of each sample).

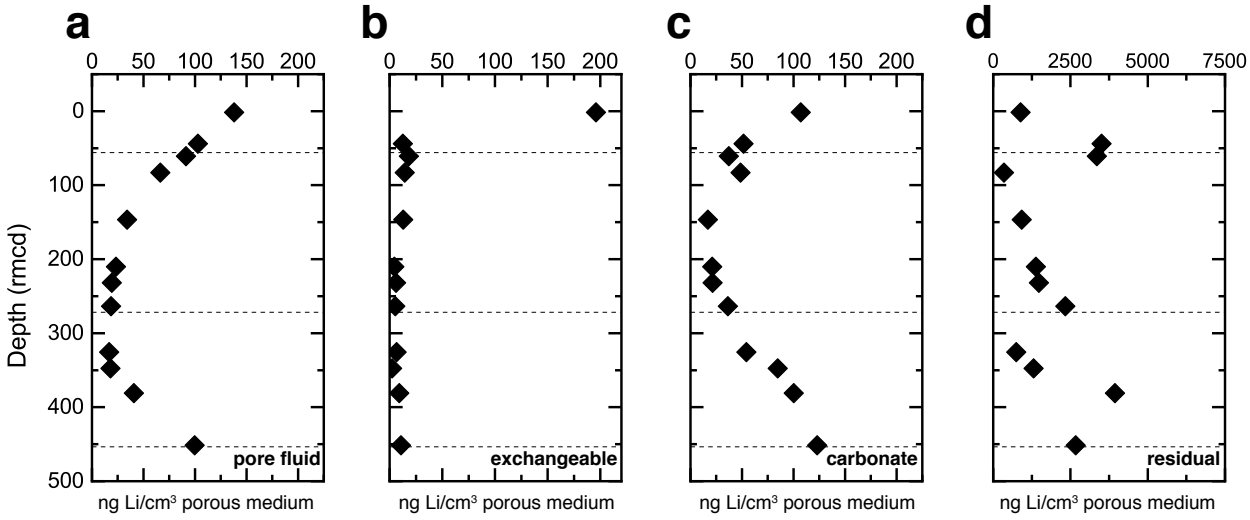

Figure 4. Concentration of Li in pore fluids and the concentration in each of the fractions of the sequential sediment leach (presented as ng Li/cm^3 porous media). (a) pore fluid concentration from Palïke et al., (2010b) for reference, (b) Li concentration in the exchangeable fraction, (c) Li concentration in the carbonate fraction, and (d) Li concentration in the residual fraction. Dashed lines denote the unit boundaries.

Generally, Li concentrations in both the exchangeable and carbonate fractions are in the range of tens to hundreds of ng Li per cm^3 sediment (i.e., comparable to those in the pore fluid; Fig. 4), while Li concentrations in the residual fraction are on the order of thousands of ng Li/cm^3 sediment (Fig. 4d). Exchangeable Li ranges from ~2 to 18 ng Li/cm^3 sediment through most of the section. The sample closest to the seawater-sediment boundary has a concentration of ~200 ng Li/cm^3 porous medium. Similarly, carbonate concentrations are relatively high at the top (~106 ng Li/cm^3) and bottom (~122 ng Li/cm^3) of the section and relatively low in between (minimum ~16 ng Li/cm^3 sediment between 150 and 250 meters).

383 Lithium concentrations in the HF-soluble residual fraction are significantly higher than
384 either the exchangeable or carbonate fractions; in the upper part of the section (Units I and II),
385 concentrations range between ~350 ng Li/cm^3 sediment and ~3,500 ng Li/cm^3 sediment at 45
386 rmcd. In Unit III, residual Li concentrations generally increase with depth; the maximum
387 concentration is ~4000 ng Li/cm^3 sediment at ~381 rmcd. The concentration of Li in the sample
388 located near the sediment-basement interface decreases to ~2700 ng Li /cm3 sediment.

389 In these sediments, between 66 and 97% of the total Li is within the silicate phase while
390 the fraction of Li in the carbonate and pore fluid phases ranges between 1 and 10%. The
391 exchangeable fraction typically contains less than 1% of the total Li in each sample except for
392 the sample closest to the seawater-sediment boundary which contains ~15% of the total Li.

393 The Li isotopic compositions of representative extractions were also measured. The
394 exchangeable fraction is enriched in ^{6}Li relative to the pore fluids (Fig. 3), ranging from 25 to
395 33‰ with no consistent offset between the pore fluid and exchangeable isotopic compositions.
396 Carbonate isotopic composition is generally similar to seawater, with values ranging between 24
397 and 33‰ and no consistent offset between carbonate and pore fluid. Carbonate δ^7Li values
398 increase somewhat with depth, though the trend is noisy. The deepest carbonate, which is located
399 closest to the sediment-basement interface, is isotopically similar to seawater. Residual samples
400 at 1.49, 44.05, and 451.56 rmcd have δ^7Li values that are significantly lower than corresponding
401 pore fluids (6-11‰), and that increase systematically with depth.

402

403 *4.3 Scanning electron microscopy (SEM)* and *X-ray diffraction (XRD)*

Scanning electron microscopy (SEM) images of the > 63 μm fraction of the bulk sediment indicate the presence of disk-shaped diatoms surrounded in a biogenic silica (radiolaria/broken diatoms) or carbonate (coccolith) matrix. The carbonate matrix largely consists of coccolithophore plates (see Fig. S2 for additional SEM images of sediment). In most of the sediments imaged, well preserved disk-shaped diatoms are observed (Fig. 5a). Energy dispersive spectroscopy (EDS) analysis (Fig. 5c) indicates that there are insignificant amounts of other cations present in the SiO_2 matrix. In some samples, the disk-shaped diatoms are coated in a material with plate-like structures (Fig. 5b). Analysis via EDS indicates that these particles are aluminosilicates with trace amounts of cations such as Fe and Mg (Fig. 5d).

Powder X-ray diffraction (XRD) analysis of several residual extractions was completed in order to identify the presence of clay minerals in the sediment, and supplement IODP smear slide data and core descriptions. Each sample displays multiple peaks at 2θ (5º to 10º) and high d-spacing (16.3 to 16.8; Fig. 5e,f), which is indicative of phyllosilicates (in particular, smectite).

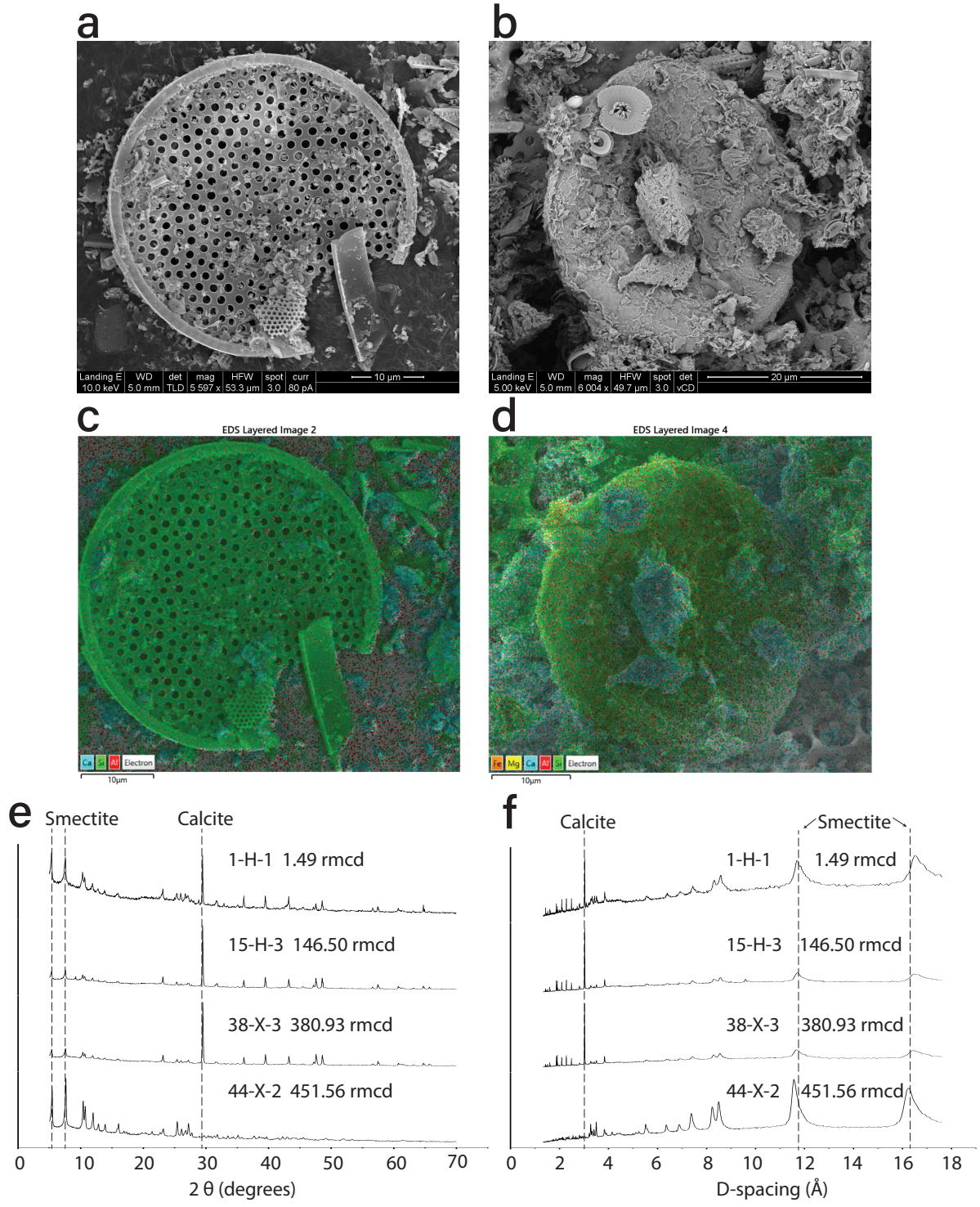

Figure 5. SEM images of sediment and XRD data. (a) SEM image of well-preserved diatom from ~146 rmcd (b) SEM image of coated diatoms from ~44 rmcd. (c) EDS data overlaying SEM image from 5a. (d) EDS data overlaying SEM image from 5b. (e) X-ray diffraction (XRD) data from Site 1338 samples 1-H-1, 15-H-3, 38-X-3, and 44-X-2 presented as a function of 2θ

and (f) d-spacing. The calcite peaks were picked using the Jade software package, and the smectite peaks identified using literature values (Chipera and Bish, 2001).

5 Discussion

The data presented in this study support the contention that clay authigenesis occurs in carbonate-rich sediments, and that this process controls the Li geochemistry of the system. In the Discussion that follows, we discuss the evidence for, and present reactive transport models that substantiate, this hypothesis. We then discuss the relevance of clay authigenesis to the global Li cycle, and present reactive transport models that highlight how this process impacts the size and isotopic composition of the authigenic sink over geologic time scales.

5.1 Evidence for chemically-relevant authigenic clay formation at Site U1338

It is clear from the aqueous Li concentration depth profile at Site U1338 that the system is not at a diffusive steady state; such a state would require that the pore fluid Li concentration profile with depth be a straight line connecting the upper and lower boundary conditions. Rather, the Li pore fluid profile is non-linear, indicating that a reactive process must be removing Li in the sedimentary column (and not at the boundaries or by mixing). To confirm that the elemental and isotopic trends are not the result of mixing, pore fluid δ^7Li values were plotted against major cation concentrations (Fig. S5). If the isotopic trends were a result of mixing, we would observe binary mixing trends between endmember fluids, such as seawater at the sediment water interface and the basement fluid at the sediment-basement boundary. However, no such trend exists between the deepest and shallowest samples. While trends exist in the pore fluid δ^7Li vs pore fluid Si concentration, pore fluid δ^7Li vs pore fluid Sr concentration, and pore fluid δ^7Li vs pore fluid Li concentration plots, these trends clearly are not related to mixing but reflect the impact of either carbonate recrystallization (Voigt et al., 2015) or clay authigenesis.

447 Several processes could act as the pore fluid Li sink, including surface exchange on clays,
448 carbonate recrystallization, and clay authigenesis. Our sequential extractions suggest that this
449 sink is neither the operationally-defined exchangeable fraction nor the carbonate fraction, as less
450 than 20% of the total Li per sample is contained in the exchangeable or carbonate fraction. While
451 one could argue that such processes occur quickly and therefore the size of the reservoir is
452 unimportant, the mass of Li in these reservoirs is a critical constraint on the potential size of the
453 isotopic effect of a given process on pore fluid δ^7Li. In addition to the mass constraint, our
454 understanding of the fractionation factors associated with exchange and carbonate
455 recrystallization suggests that neither explain pore fluid δ^7Li at Site U1338.

456 Exchange, for instance, occurs quickly relative to the time scale over which the system
457 evolves, such that a mixing equation is suitable for elucidating its impact on pore fluid δ^7Li:

458 $$\delta^7 Li_{pf} = \delta^7 Li_{sw} - X_{exchange} \cdot \Delta^7 Li_{exchange-pf} \quad [2]$$

459 where *pf* refers to pore fluid Li reservoir and *exchange* to the surface exchangeable reservoir,
460 $\Delta^7 Li_{exchange-pf}$ is the fractionation factor associated with exchange, X_i is the mole fraction of
461 Li in the i^{th} reservoir, and we assume that the Li isotopic composition of the system is that of
462 modern seawater (*sw*). According to Eq. 2, exchange can only have a sizeable effect on pore
463 fluid $\delta^7 Li$ if the fraction of Li exchanged is large and the fractionation factor is sizeable. At
464 Site U1338, exchange has neither the mass nor isotopic leverage to explain the pore fluid data.

465 Though carbonate recrystallization requires a different quantitative approach (e.g.,
466 Richter and DePaolo, 1987), neither the pore fluid nor the carbonate δ^7Li values are consistent
467 with either carbonate recrystallization or net carbonate precipitation as the controlling process,
468 based on the 6‰ fractionation observed between seawater and core-top carbonates (Pogge von

469 Strandmann et al., 2019b) and the fractionation factors associated with experimentally-
470 precipitated carbonate (~3-6‰; Marriott et al., 2004b; Marriott et al., 2004a). The rate of
471 recrystallization and the elemental partitioning of Li into the diagenetic phase must also be
472 considered, and we discuss this topic below in more detail.

473 By contrast, the residual HF-soluble fraction, which we assume samples the authigenic
474 contribution (in addition to any detrital component), has a Li concentration that is two orders of
475 magnitude larger than the other reservoirs (Fig. 4). Further, the isotopic fractionation associated
476 with clay formation ($\alpha_{clay-fluid} \approx 0.972$-$0.985$) is sizeable and, combined with the assumption of
477 the mass flux associated with clay authigenesis, can explain the pore fluid δ^7Li data.

478 A range of supplemental evidence supports the contention that Li is removed by clay
479 authigenesis at Site U1338. Clay formation preferentially incorporates ^{6}Li (Pistiner and
480 Henderson, 2003; Vigier et al., 2008; Wimpenny et al., 2015), increasing pore fluid δ^7Li values
481 in fluids that are not in diffusive communication with either the upper or lower boundaries. At
482 Site U1338, pore fluid δ^7Li values are considerably higher at depth relative to seawater; the
483 highest delta value is ~52‰ at 325 rmcd (or ~20‰ higher than seawater). Additional evidence
484 for clay formation is the low δ^7Li value of the residual phase (Fig. 3). As we will discuss in more
485 detail below, an increase in pore fluid δ^7Li with depth in the sedimentary section is expected due
486 to clay authigenesis.

487 In addition, while smear slide observations suggest that the residual fraction consists of
488 diatoms and radiolaria (Palïke et al., 2010b), the measured Li concentrations in the HF residual
489 fraction cannot be explained by biogenic silica, which is assumed to have Li concentrations less
490 than 2 ppm (Chan and Kastner, 2000). All of the residual samples have concentrations greater

than 2 ppm, strongly suggesting the presence of an HF-soluble siliciclastic phase in addition to biogenic silica and detrital clay. Authigenic clays can have Li concentrations of 50-100 ppm with a maximum concentration of ~500 ppm Li (Hein et al., 1979; Chan et al., 2006; Vigier et al., 2008), nearly an order of magnitude larger than the Li concentration in detrital clays (Zhang et al., 1998).

We estimate the relative contribution of each component by mass balance using the mass of Li in the residual fraction measured at Site U1338 and assuming Li concentrations in the biogenic silica (2 ppm) and authigenic (500 ppm) or continentally-derived/detrital (50 ppm) clay endmembers (Table 1). Given these assumptions, the maximum proportion of authigenic clay ranges from ~1-5% throughout the section. If continentally-derived clay is the only component that is mixed with biogenic silica, then the maximum proportion of detrital clay is 40%. We conclude that this value is too high to have been missed in smear slide observations, and thus suggest that this supports the contention that the Li geochemistry reflects the presence of authigenic clay at Site U1338. Though detrital clays may be present in the section, we contend that they do not explain the Li geochemical trends that we observe.

Altogether, the data presented above support the contention that biogenic silica (mainly diatoms) facilitates the precipitation of authigenic clay minerals at Site U1338. Such a hypothesis is consistent with studies of coastal sediments near the Amazon River outflow, which inferred a similar process to be occurring (Michalopoulos et al., 2000; Michalopoulos and Aller, 2004). Our observations, however, indicate that this process is not restricted to shallow deltaic sediments but could also be important in deep-sea carbonate sediments. Such a hypothesis has a range of implications for proxy archives and the global Li cycle, which we discuss in detail below.

514 A reactive transport modeling approach was utilized to evaluate whether or not
515 authigenic clay formation is appropriate for explaining the observed Li and SiO_2(aq)
516 concentration and Li isotopic profiles. The model takes into account gross differences in porosity
517 and amorphous silica (SiO_2(am)) concentration with depth in the column (i.e., between Units I/II
518 and Unit III). In all simulations shown (Fig. 6), the fractionation factor associated with diffusion
519 is 0.9982, burial is assumed to be constant (=23.7 m Ma^{-1}), and the initial pore fluid Li
520 concentration and δ^7Li is 26 μm and 31.5‰, respectively. The authigenic solid is assumed to be
521 unreactive after precipitation, and the lower boundary is open to diffusion. The model is run for
522 10.6 Ma, and is initially comprised of a 450-meter section that has similar porosity (0.634) and
523 biogenic silica content (10.8 wt. %; 2 ppm Li) as Unit III (89.2 wt. % Li-free carbonate). The
524 simulation then buries the initial sediments with sediment that has a porosity of 0.767, a biogenic
525 silica content of 23.8 wt. %, and a carbonate content of 79.2 wt. % (i.e., similar to Units I and II).
526 During the simulation, biogenic silica dissolves and reprecipitates as an authigenic clay mineral
527 that has a Li concentration of 500 ppm, with variable $\alpha_{clay-fluid}$ (in these simulations, we create a
528 "basecase" simulation for comparison where $\alpha_{clay-fluid}$ is 0.986; Pistiner and Henderson, 2003).
529 As there is no constraint on the identity of the authigenic phase forming at Site U1338, and no
530 pore fluid Al data are available, we have chosen an authigenic clay phase (hectorite) that consists
531 of Si, Na, Mg, and Li ($4H_2O + 4SiO_2(aq) + 0.03Li^+ + 0.03Na^+ + 2.97\ Mg^{++} \rightarrow$
532 $(Mg,Li,Na)_3Si_4O_{10}(OH)_2 + 6H^+$). Saturation state calculations indicate that the pore fluid is
533 supersaturated with respect to this mineral at all depths.
534 Generally, the model reproduces the major features of the Li concentration and isotopic
535 profiles. However, the Li isotopic composition of the pore fluid in Unit III is poorly fit when we
536 assume a fractionation factor of ~0.986, an average of fractionation factors associated with

537 secondary mineral precipitation and, more generally, basalt interaction with seawater (0.972 to
538 0.999; Chan et al., 1992; Pogge von Strandmann et al., 2008; Wimpenny et al., 2015) and
539 comparable to that associated with smectite precipitation at low temperatures (0.990 ± 0.0013;
540 Vigier et al., 2008), and equal reactivity of authigenic clay in the upper and lower units (Fig. 6a).
541 In this case, the term 'reactivity' refers to the fundamental controls on authigenic precipitation
542 rate aside from saturation state (i.e., surface area and intrinsic rate constant). In light of this
543 discrepancy, there are two likely means by which the pore fluid δ^7Li trend with depth at Site
544 U1338 can be explained: (i) an increase in authigenic clay reactivity in Unit III or (ii) a
545 fractionation factor that varies with depth. The observed discrepancy can also be explained by a
546 different Li stoichiometry in the authigenic clay in Units I/II and Unit III, though this is an effect
547 that we do not attempt to simulate given the lack of constraints on the composition of the
548 authigenic phase.

549 An increase in authigenic clay reactivity by ~20x in Unit III relative to Units I/II is
550 sufficient to explain the Li isotopic composition of the pore fluids (Fig. 6b). In the model, the
551 reactivity increase is generated by an increase in the specific surface area of the precipitating
552 clay in Unit III, though the overall precipitation rate is a function of both the saturation state and
553 rate constant as well as specific surface area. In the enhanced reactivity scenario (Fig. 6b), the
554 model precipitation rates were generally higher by no more than a factor of 2 in Unit III
555 compared to Units I/II, though this difference varied as a function of the saturation state with
556 depth. Our observation is that enhanced reactivity is consistent with the Li concentration profile
557 and, while the pore fluid Li concentration profile is slightly less well fit in Units I/II, the
558 asymmetry of the depth trend is captured.

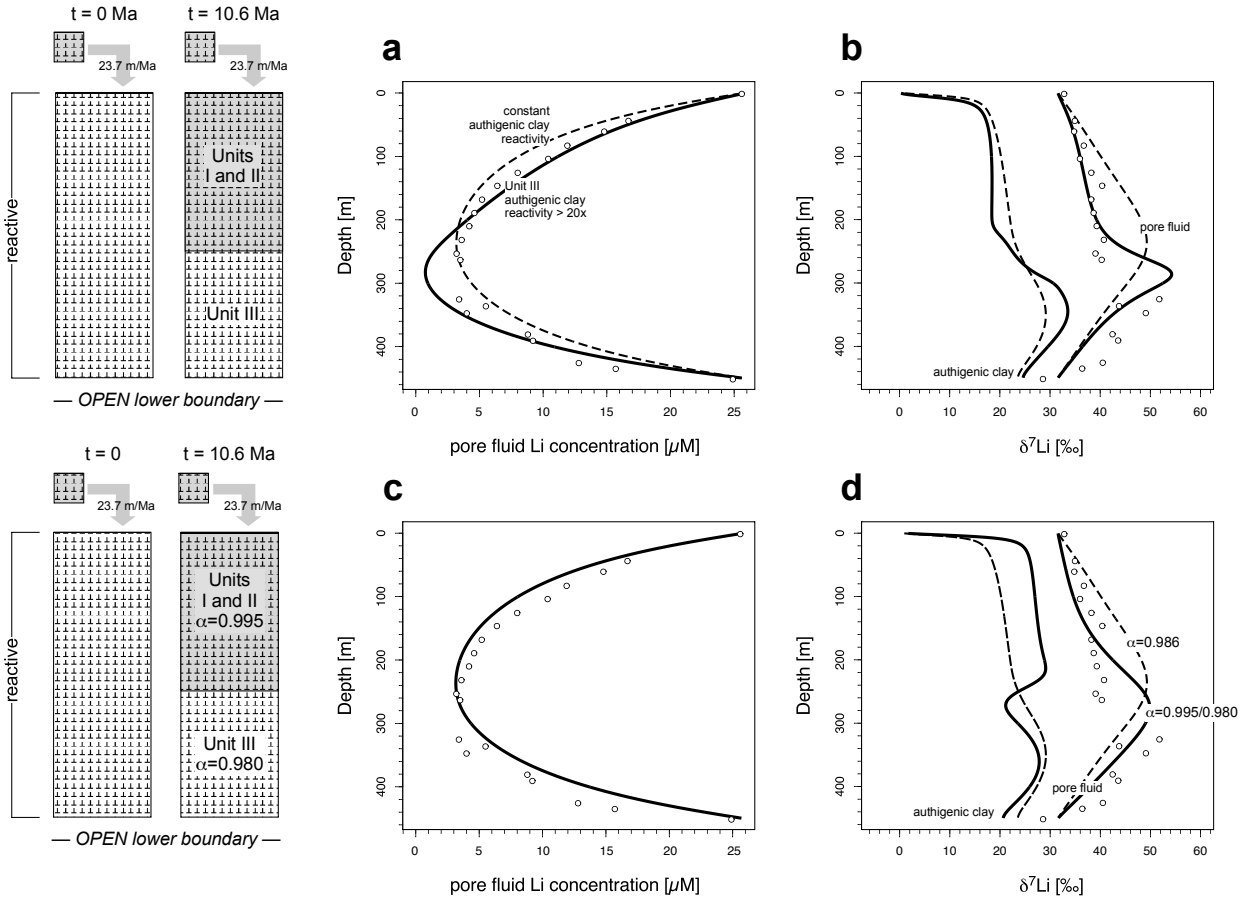

Figure 6. Reactive transport simulations of the burial of Unit III over 10.6 Ma at Site U1338 assuming two scenarios: (a-b) a change in authigenic clay reactivity between Units I/II and Unit III and its impact on (a) pore fluid Li concentration and (b) δ^7Li of pore fluid and authigenic solid; (c-d) a change in the fractionation factor associated with authigenic clay precipitation in Unit III and its impact on (a) pore fluid Li concentration and (b) δ^7Li of pore fluid and authigenic solid. In (d), the thicker black curves refer to authigenic clay formed in Units I/II and the gray curves refer to the authigenic clay formed in Unit III. In (a-b), the term 'reactivity' refers specifically to a 20x difference in specific surface area (m^2/g) between authigenic clay in Unit III and authigenic clay in Units I/II; the intrinsic rate constants associated with authigenic clay precipitation are the same for both units, as are the fractionation factors associated with authigenesis ($\alpha_{clay-fluid}$). Because precipitation rate is a function of surface area, the intrinsic rate constant, and the saturation state, the 20x difference in surface area does not necessarily correlate with a 20x different in precipitation rate. Precipitation rates in the 20x scenario are generally no more than twice those in the 'equal reactivity' scenario (i.e., equal specific surface area).(Pistiner and Henderson, 2003)

A different fractionation factor between Units I/II and Unit III can also explain the pore fluid δ^7Li trend with depth. If the fractionation factor is ~0.995 in Units I/II and ~0.980 in Unit

III, the general shape of the depth trend can be approximated (Fig. 6d). Such values are generally consistent with Li isotopic fractionation associated with secondary mineral formation, but are significantly different from experimental constraints on fractionation associated with smectite precipitation (Hindshaw et al., 2019). We stress that our constraint on the fractionation factor is general; we do not know the mineralogy of the precipitating phases nor have we simulated carbonate recrystallization and clay authigenesis together.

Nonetheless, the critical observation we make in comparing the two hypotheses is that it is difficult to match the sharpness of the δ^7Li profile by varying the fractionation factor, unlike in the case of faster clay precipitation rates in Unit III. This is because the balance between diffusion and reaction, which is constrained by the Li concentration trend with depth, is the same in Units I/II and Unit III in the case of variable fractionation factor, unlike the variable reactivity scenario. As the rates of clay precipitation and biogenic silica dissolution increase, the diffusive reaction length scale decreases and allows for the maintenance of steeper concentration and isotopic gradients. Thus, we contend that the features of the δ^7Li pore fluid profile support the hypothesis that authigenic clay precipitation rates are significantly higher in Unit III relative to Units I/II.

Overall, the modeling suggests that authigenic clay formation can explain the Li elemental and isotopic geochemistry at Site U1338. Our simulations are consistent with ~1 vol. % authigenic clay in Site U1338 carbonate sediments, but this value will vary if the stoichiometry of the authigenic phase that we assume to be forming changes. In addition, it is notable that reactivity changes in the sedimentary column complicate efforts to constrain mineral-aqueous fractionation factors from pore fluid data. Using Site 1338 as an example, one could interpret the change in pore fluid δ^7Li as reflecting a change in fractionation factor (and

601 thus process and/or mineralogy), when it could simply reflect a change in mineral reactivity at
602 depth (which does not require a change in process). The interpretations in these two cases are
603 thus entirely distinct.

604

605 *5.2 Implications of authigenic clay formation in carbonate-rich sections for the global Li cycle*

606 If marine authigenic clay formation is important globally, then this process can, in some
607 cases, generate a significant flux that removes Li from the ocean. This is due to the fact that
608 authigenic clay minerals can incorporate hundreds of micrograms of Li per gram of clay (Hein et
609 al., 1979), compared to the tens of μg Li/g clay typical in detrital clays (Zhang et al., 1998). Clay
610 authigenesis, therefore, has the potential to impact the global Li cycle (Chan et al., 1992; Chan et
611 al., 2002; Hathorne and James, 2006). In order to estimate the size of such a flux, we explore Li
612 pore fluid concentration gradients throughout the modern ocean and attempt to outline the major
613 controls on those gradients. Our objectives are to predict how such a flux might change over
614 geologic time scales and to discuss what may drive such changes.

615

616 *5.2.1 Controls on the Li concentration gradient in marine pore fluids*

617 The global Li cycle is often considered to be at steady state (Stoffyn-Egli and Mackenzie,
618 1984; Huh et al., 1998; Hathorne and James, 2006; Misra and Froelich, 2012), and the reverse
619 weathering flux calculated as a consequence of this assumption. Of the major inputs of Li to the
620 modern ocean, the riverine flux has been estimated to be between $8 \cdot 10^9$ moles Li/a (Huh et al.,
621 1998) and $1 \cdot 10^{10}$ moles Li/a (δ^7Li ~ 23‰) (Misra and Froelich, 2012). The hydrothermal flux
622 has been estimated to be between $6 \cdot 10^9$ moles Li/a (Hathorne and James, 2006) and $1.3 \cdot 10^{10}$

623 moles Li/a (δ^7Li ~ 8.3‰) (Misra and Froelich, 2012), and the subduction reflux has been
624 estimated to be ~$0.6 \cdot 10^{10}$ moles Li/a (δ^7Li ~15‰) (Misra and Froelich, 2012). The total input
625 flux thus ranges between ~$1.4 \cdot 10^{10}$ and $2.9 \cdot 10^{10}$ moles Li/a (Hathorne and James, 2006; Misra
626 and Froelich, 2012).

627 Lithium is removed from the modern ocean via the formation of secondary silicate
628 minerals in the sedimentary column or during the alteration of basalts. To maintain steady state,
629 these output fluxes must be on the order of 10^{10} mol Li/a. Little appears to be known about how
630 the output flux is apportioned in the modern ocean, and what controls the distribution between
631 the two main sinks; it has been suggested that the two sinks in the modern ocean are
632 approximately equivalent and that shifts between them can account for at least some of the
633 variability in the evolution of seawater δ^7Li over the Cenozoic (Li and West, 2014). Insight into
634 the controls on these sinks is critical, as it allows us to infer how such fluxes may vary over
635 geologic time scales and, therefore, to evaluate how reasonable hypotheses invoking authigenic
636 shifts may be. Because these inferences are crucial to interpreting the Li isotope proxy, we
637 explore the marine authigenic sink in some detail.

638 In the modern ocean, Li concentration profiles in marine sections generally either
639 decrease with depth or increase with depth (Fig. 7b-d), a feature that is generally dictated by the
640 balance between detrital silicate dissolution and authigenic clay precipitation. Profiles that
641 decrease with depth are observed in carbonate-rich sediments and volcanogenic sediments (Fig.
642 7b; e.g., Zhang et al., 1998; You et al., 2003). Profiles that increase with depth are often found in
643 terrigenous and convergent margin sediments, in which the Li dissolution flux exceeds the
644 precipitation flux (Fig. 7c; e.g., Martin et al., 1991; You et al., 1995; Zhang et al., 1998; Chan
645 and Kastner, 2000). To begin to understand the distribution of these profiles and their impact on

646 the global Li cycle, a survey of Li concentration profiles and lithology (mainly % $CaCO_3$) was
647 conducted. Our general finding is that pore fluid Li concentration trends with depth are steepest
648 at sites with high $CaCO_3$ contents (decreasing with depth), while there is considerably more
649 variability at sites where siliciclastic contents are higher. This observation is consistent with the
650 control of Li pore fluid concentration gradients by lithology.

651 A compilation of all ODP and IODP sites with Li concentration data extending more than
652 50 meters below seafloor suggests that Li sinks are distributed globally throughout the ocean.
653 (Fig. 7a). Of the 267 sites that were categorized, 78 sites are sinks, 60 sites are sources of Li to
654 the ocean, and 129 are hybrids that have low to sink-like slopes in the upper 50-100 meters but
655 increase in concentration at depth. It is unclear if the hybrid sites are at steady state, a topic we
656 address below. Broadly speaking, sink sites are located in the open ocean, while both source and
657 hybrid sites are typically located close to land/continental margins (Fig. 7a). The geographical
658 distribution generally supports the hypothesis that sink sites are a consequence of dominant
659 secondary mineral precipitation relative to silicate dissolution; ostensibly, this is a consequence
660 of low terrigenous input relative to biogenic silica input in the open ocean. The sites that act as
661 sinks near continental margins and in siliciclastic sediments have previously been discussed
662 (e.g.,. Stoffyn-Egli and Mackenzie, 1984 and Zhang et al., 1998) and will not be discussed
663 further here.

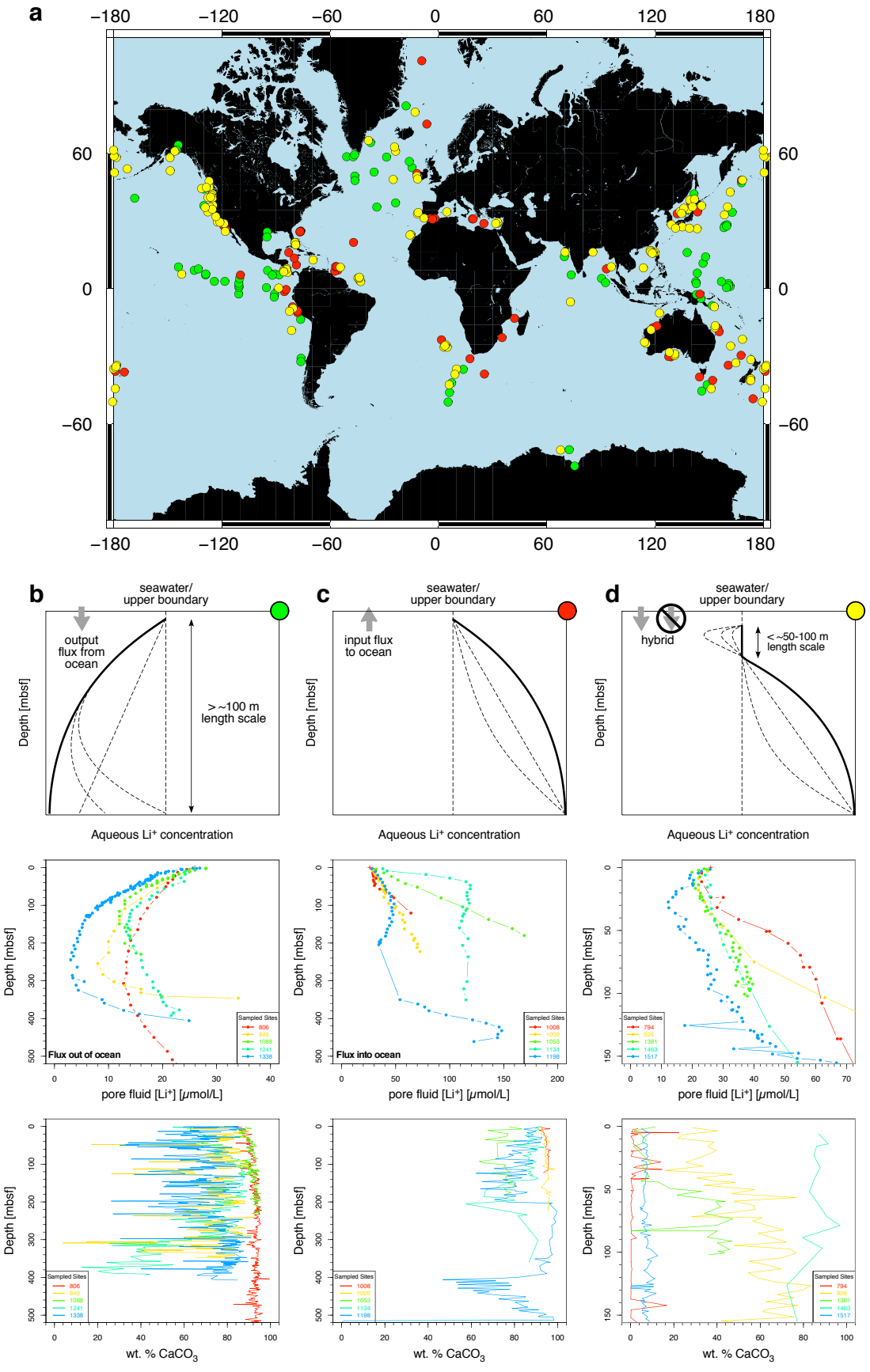
a
−180
−120
−60
0
60
120
180
60
0
−60
b
seawater/
upper boundary
output
flux from
ocean
> ~100 m
length scale
Depth [mbsf]
Aqueous Li⁺ concentration
c
seawater/
upper boundary
input flux
to ocean
Depth [mbsf]
Aqueous Li⁺ concentration
d
seawater/
upper boundary
hybrid
< ~50-100 m
length scale
Depth [mbsf]
Aqueous Li⁺ concentration
Depth [mbsf]
Flux out of ocean
Sampled Sites
806
849
1088
1241
1338
pore fluid [Li⁺] [μmol/L]
Depth [mbsf]
Flux into ocean
Sampled Sites
1008
1009
1053
1134
1198
pore fluid [Li⁺] [μmol/L]
Depth [mbsf]
Sampled Sites
794
926
1381
1463
1517
pore fluid [Li⁺] [μmol/L]
Depth [mbsf]
Sampled Sites
806
849
1088
1241
1338
wt. % CaCO3
Depth [mbsf]
Sampled Sites
1008
1009
1053
1134
1198
wt. % CaCO3
Depth [mbsf]
Sampled Sites
794
926
1381
1463
1517
wt. % CaCO3

664

Figure 7. Compilation of pore fluid Li concentration gradients in the modern ocean at a range of ODP and IODP sites. (a) Map summary of sites that have positive (red), negative (green), or hybrid (yellow) gradients over the upper 50-100 meters of the section. Examples of sites that have (b) decreasing/negative, (c) increasing/positive, and (d) hybrid Li concentration profiles with depth. The latter typically exhibit sink profiles over ~50-100 meters at the top of the section, but increase below this depth to Li concentrations that are usually greater than the modern seawater Li concentration (i.e., 26 μM). Also noted in the lowermost row of panels is the $CaCO_3$ content of each site as a function of depth.

Ultimately, we hypothesize that carbonate-rich sediments exhibit Li concentration profiles that decrease with depth because the flux of Li into precipitating authigenic clays is greater than the flux from dissolving carbonate, detrital clays and/or biogenic silica. Accordingly, Li concentration gradients in carbonate-rich sediments have the potential to be steep, and carbonate-rich sediments could therefore be significant Li sinks from the ocean within the global Li cycle.

5.2.2 Quantifying the Li sink in carbonate-rich sediments and assessing its secular variability

To elucidate the importance of this diffusive flux within the global Li cycle, and to assess those factors that may drive secular variability in this output flux, we utilized simple calculations and reactive transport simulations to estimate the size and isotopic composition of the global output flux of Li as well as the secular evolution of the flux. Diffusive mass fluxes (F, in units of moles per unit area per time) calculated from pore fluid Li concentration profiles using Fick's First Law ($F = -\emptyset \cdot D \cdot dC/dz$, where $D = 6.84 \cdot 10^{-6}$ cm^2/s; e.g., Berner, 1980) ranged from $1.4 \cdot 10^{-6}$ to $4.5 \cdot 10^{-4}$ mol $Li/m^2/a$, depending on the length scale over which the Li concentration gradient was imposed (1 to 250 m) and the porosity (0.6 to 0.8), If we consider seawater Li

concentrations as much as five times the modern value, then the flux estimates increase to ~$6.7 \cdot 10^{-6}$ to $2.2 \cdot 10^{-3}$ mol Li/m^2/a.

If we assume that this mechanism operates in carbonate sediments over the entire surface area of the ocean (excluding continental shelves: ~$3.1 \cdot 10^8$ km^2), the *maximum* removal flux in carbonate sediments is ~$1.4 \cdot 10^{11}$ moles Li/a assuming a porosity of 0.8 and a seawater Li concentration of 26 μM ($F = 7 \cdot 10^{11}$ mol Li/a if we assume 5x modern Li seawater concentration). If we assume a porosity of 0.7 and the maximum concentration gradient (i.e., from 26 μM to 0) over 10-100 meters, then the flux estimate is ~$1.2 \cdot 10^9$ to $1.2 \cdot 10^{10}$ mol Li/a, which is comparable to the total removal flux cited by Hathorne and James (2006) and Misra and Froelich (2012). With regard to the modern ocean (26 μM, $1.46 \cdot 10^{21}$ kg, $3.8 \cdot 10^{16}$ mol Li), this equates to a ~3-30 Ma time scale ($\tau = N/F$, where N is the moles of Li in the ocean and F is the flux in mol/Ma) over which this flux impacts the isotopic evolution of the ocean.

More interestingly, the output mass flux and isotopic composition of this flux may vary over time, a feature that we illustrate using reactive transport simulations. In particular, the secular variability in the isotopic composition of the authigenic output flux is controlled by the depth in the sedimentary column at which, and the extent to which, Li precipitates in clays. In the model simulations, this is illustrated by two scenarios in which reactive SiO_2(am) is buried and dissolves in the sedimentary column, generating a chemical drive to precipitate authigenic clay (Fig. 8). In the first scenario, reactive SiO_2(am) is buried continuously from 2.5 Ma to 20 Ma; in the second scenario, the reactive zone is discrete and moves through the column as burial occurs at the upper boundary. The two scenarios yield considerable differences in pore fluid geochemistry, some of which are due to the fact that the rate constants are the same for the

712 reactive zones in both cases but the size of the reactive zones is different between the two cases,
713 resulting in a considerable difference in the amount of integrated reaction in the two scenarios.

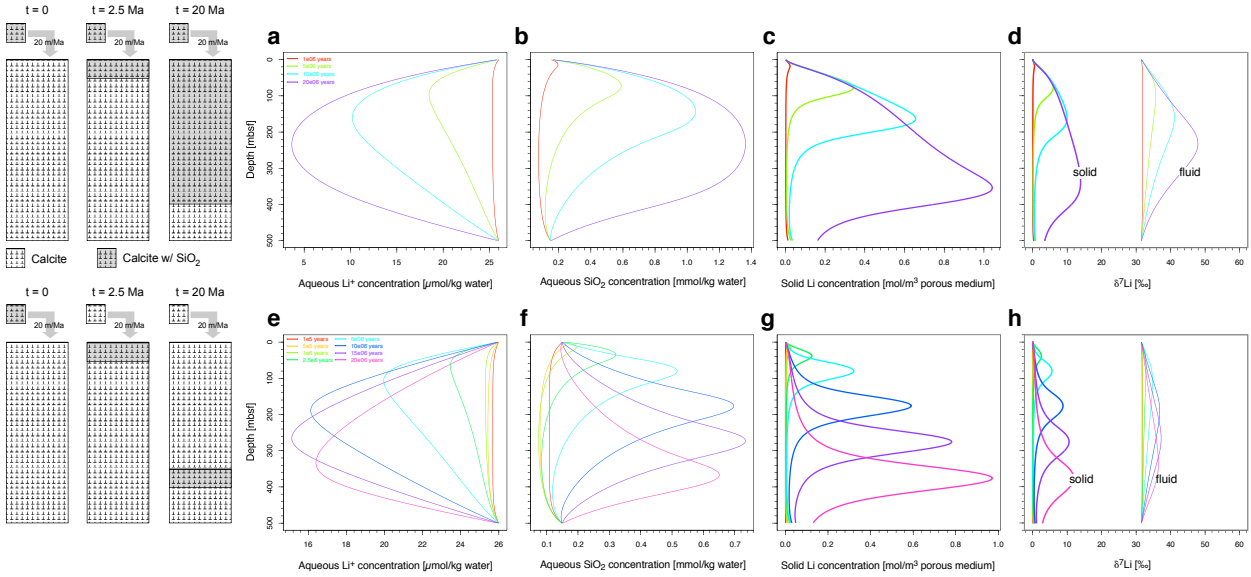

714

715 Figure 8. Generic reactive transport model simulations of pore fluid Li concentration and
716 isotopic composition for two cases: (i) continuous and (ii) discrete deposition and burial of
717 reactive silica. Case (i) simulations are shown in panels (a-d), while Case (ii) simulations are
718 shown in panels (e-h). In each row, from left to right, the parameters depicted are: pore fluid Li^+
719 concentration, pore fluid $SiO_2(aq)$ concentration, authigenic solid Li concentration, and pore
720 fluid and authigenic solid δ^7Li.
721

722 Regardless, the models clearly support the contention that isotopic distillation, due to
723 isotopic fractionation associated with clay precipitation, occurs in the pore fluid at depth if the
724 solid does not back-react (or back-reacts slowly) with the pore fluid. Distillation is most
725 pronounced far from boundaries, such as the seawater-sediment and sediment-basement
726 interfaces, where diffusive input of Li to the pore fluid is unable to keep pace with Li removal by
727 clay precipitation (e.g., Fantle et al., 2020). The effect of distillation at depth in the sedimentary
728 column is to generate an output flux that is isotopically closer to seawater than would be
729 assumed on the basis of experimental fractionation factors. For instance, the isotopic

730 fractionation associated with the "reverse weathering" output flux has been cited as ranging
731 between -14 and -16‰, based (at least in part) on isotopic fractionation factors constrained by
732 laboratory experiments (e.g., Pistiner and Henderson, 2003; Vigier et al., 2008; Hindshaw et al.,
733 2019). Our simulations suggest that this constraint may not accurately reflect the bulk of the
734 authigenic output flux, and that isotopic distillation at depth modifies the effective fractionation
735 factor of the output flux. Such fractionation factors would explain authigenesis occurring near
736 the seawater-sediment interface, but that is likely negligible.

737 The simulations suggest a predictable and systematic means by which the isotopic
738 composition and size of the authigenic output flux may vary over time. In the continuous burial
739 scenario (Fig. 8a-d; Fig. 9a), the mass output flux increases in time as more reactive biogenic
740 silica is buried. As a consequence, the pore fluid Li concentration gradient steepens and the
741 diffusive mass flux of Li out of the ocean increases. At the same time, the extent of isotopic
742 distillation increases, as the integrated depth over which authigenesis occurs also increases.
743 Thus, the isotopic composition of the output flux becomes less fractionated relative to seawater,
744 reducing the leverage of authigenesis to change seawater δ^7Li. In the discrete burial scenario
745 (Fig. 8e-h; Fig. 9b), the zone of authigenesis moves steadily away from the sediment-seawater
746 interface, increasing the length scale of communication with the overlying water column. At a
747 given mass flux, this generates considerably more distillation than in the continuous burial case,
748 which has reactive solid over a range of depths (some of which are close to seawater-sediment
749 boundary and some of which are farther).

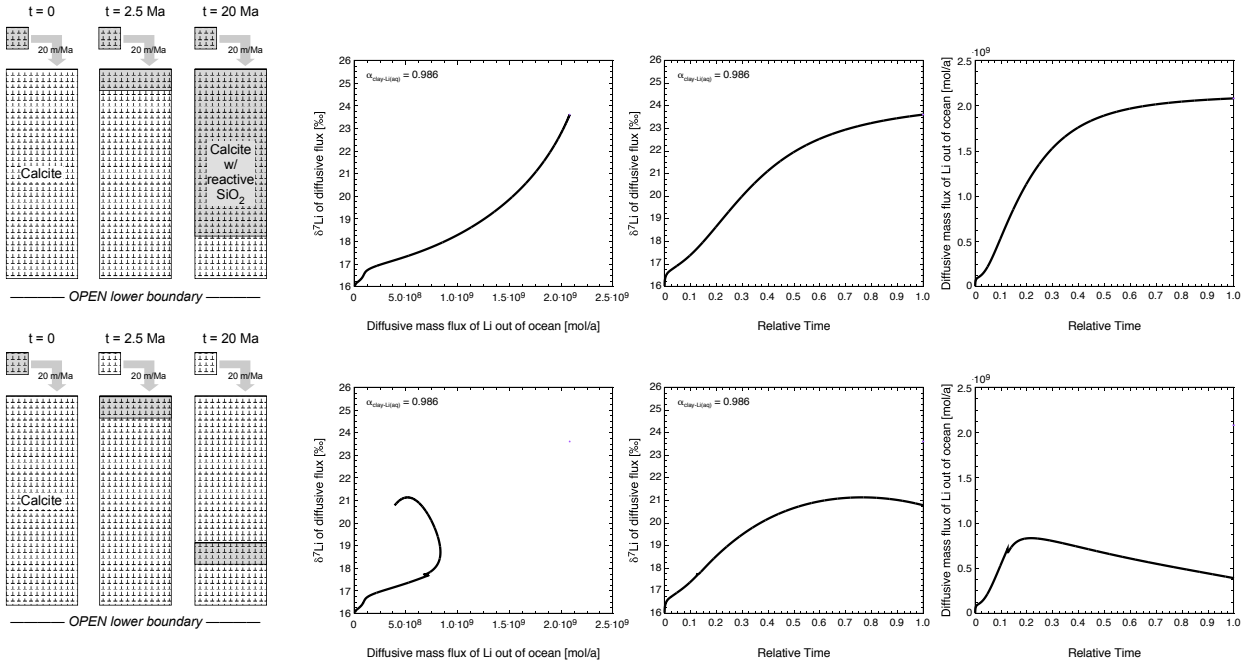

Figure 9. Calculated δ^7Li of diffusive flux of Li out of the ocean, as a function of the diffusive mass flux, for the (a) continuous and (b) discrete deposition and burial scenarios described in Fig. 8. The diffusive mass flux is a maximum estimate determined assuming authigenesis occurs over a surface area of $3.10 \cdot 10^8$ km^2 (deep-sea only, no continental shelves; e.g., Turcotte and Schubert, 1982)

Ultimately, we have shown that the Li isotopic composition of the output flux associated with clay authigenesis is not simply related to experimental fractionation factors, but is altered by isotopic distillation in the sedimentary column. Consequently, the δ^7Li value of this flux can vary in time as a function of the depth in the sedimentary column where authigenesis occurs and the relative mass of Li removed from the pore fluid. Given the significant size of the mass flux, this mechanism should be considered when interpreting secular trends of seawater δ^7Li.

5.3 Implications of clay authigenesis for the use of Li isotopes as a geochemical proxy

765 The current study has implications for the interpretation of the Li isotope proxy in
766 carbonate archives. Carbonate recrystallization in the presence of pore fluid with non-seawater
767 δ^7Li values can shift the δ^7Li of the carbonate (Fantle and DePaolo, 2007; Fantle and Higgins,
768 2014; Fantle, 2015):

769 $$d\delta_{solid} = -R\left[\left(\delta_{solid} - \delta_{fluid}\right) - \Delta_{s-f}^{diag}\right]dt \quad [3]$$

770 where $d\delta_{solid}$ is the change in the isotopic composition of carbonate mineral as a consequence of
771 recrystallization (at a given rate, *R*) at isotopic disequilibrium ($\left(\delta_{solid} - \delta_{fluid}\right) - \Delta_{s-f}^{diag} \neq 0$)
772 over time (*dt*). The term Δ_{s-f}^{diag} is the fractionation factor between carbonate solid (*s*) and the
773 aqueous species in the fluid (*f*) under diagenetic conditions, which may differ from that
774 associated with formation.

775 Diagenetic recrystallization can impact the Ca and Mg isotopic composition of
776 carbonates (Fantle and Higgins, 2014; Chanda and Fantle, 2017), as well as the $^{87}Sr/^{86}Sr$ ratio
777 (Fantle, 2015; Chanda and Fantle, 2017). Lithium may be particularly susceptible to alteration,
778 as its diffusive reaction length ($\sqrt{D/RMK}$, where *D* is the diffusion coefficient, *R* is the
779 recrystallization rate, *M* is the solid/fluid mass ratio, and *K* is the elemental partition coefficient)
780 is relatively long (~600 m) compared to other carbonate-relevant elements such as Ca (~15 m)
781 and Sr (~150 m) (Fantle and DePaolo, 2006; Fantle et al., 2020). Despite the importance of
782 understanding the impact of recrystallization on the Li isotopic composition of carbonate
783 archives that are the basis for paleoclimatic and paleoenvironmental reconstructions, there are
784 few studies of this type (Ullmann et al., 2013; Dellinger et al., 2020).

We investigate the hypothesis that recrystallization can explain bulk carbonate δ^7Li at Site U1338 using a depositional carbonate recrystallization model that has been described previously (e.g., Fantle and DePaolo, 2006). In our simulations, we assume initial Li concentrations of deposited carbonate (<30 μmol/kg solid) and recrystallization rates constrained by our modeling of Sr and Sr isotopes $\left(Fig.S3;\ rate\ [g\ reacted\ g\ solid^{-1}\ Ma^{-1}] = 0.07 \cdot e^{-age/5.25}\right)$ that are consistent with those of Voigt et al. (2015). The model simulations suggest that it is not possible to explain the bulk carbonate Li geochemistry as a consequence of recrystallization alone (Fig. 10). In addition, at these recrystallization rates, and assuming a diagenetic fractionation factor of ~0.9955 (Marriott et al., 2004b; Marriott et al., 2004a), neither the pore fluid Li concentrations (Fig. 10a) nor δ^7Li values (Fig. 10b) can be explained, even considering a large range in the partition coefficient ($K_{d,Li} = (m_{Li}/m_{Ca})_{solid}/(m_{Li}/m_{Ca})_{aq}$ = $3 \cdot 10^{-3}$ to $3 \cdot 10^{-2}$). Carbonate recrystallization alone is also not sufficient to explain the bulk carbonate (i) Li concentration (Fig. 10c-d) or (ii) Li isotopic composition trends with depth (Fig. 10e-f).

Though we cannot say with certainty what the Li concentration of primary bulk carbonate is in the section, a simple mass balance analysis suggests that the Li concentration of primary bulk carbonate is not a uniform ~40 μmol/kg with depth (i.e., similar to sediments at the top of the section):

$$\boxed{\left(\frac{N^{Li}}{N^{Ca}}\right)_{meas\ carb} = X^{Ca}_{primary}\left(\frac{N^{Li}}{N^{Ca}}\right)_{primary} + X^{Ca}_{recrystallized}\left(\frac{N^{Li}}{N^{Ca}}\right)_{recrystallized}} \quad [4]$$

where, N^i/N^j is the molar ratio of element *i* to element *j*. If we assume a primary Li/Ca of ~4 μmol/mol in bulk carbonates, then we must explain measured Li/Ca as low as 1. Yet, assuming a theoretical minimum $K_{d,Li}$ of 0, mass balance limits the recrystallized bulk carbonate to a

minimum Li/Ca of 2.4. Values lower than 2.4 must be explained by alternate means. Therefore, we contend that the initial Li/Ca of the nannofossil ooze at Site U1338 is actually ~0.1 (<10 µmol/kg solid), which is considerably lower than other biogenic carbonates (Dellinger et al., 2018).

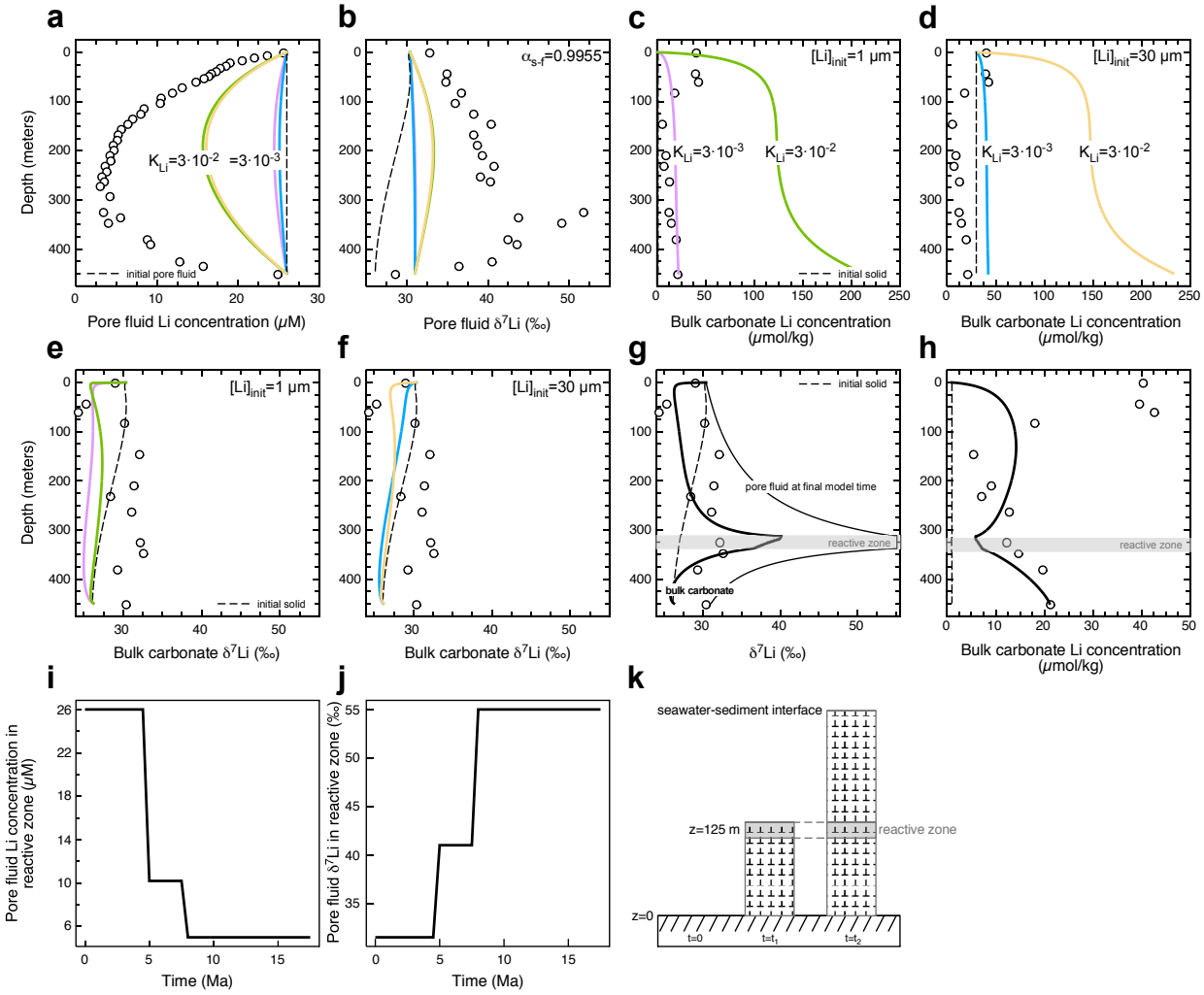

Figure 10. Model output from depositional reactive transport model (e.g., Fantle and DePaolo, 2006). For the carbonate recrystallization-only scenario, the modeled (green, yellow, blue, and pink curves) and measured (○) (a) pore fluid Li concentrations (µM), (b) pore fluid δ^7Li values (‰), bulk carbonate Li concentrations (µmol/kg) when the initial Li concentration is (c) 1 µmol/kg or (d) 30 µmol/kg, and bulk carbonate δ^7Li values (‰) when the initial Li concentration is (e) 1 µmol/kg, or (f) 30 µmol/kg. In panels (a) through (f), the partition coefficient for Li in the bulk carbonate (K_{Li}) is varied from $3\cdot10^{-3}$ to $3\cdot10^{-2}$, as indicated in (a), (c), and (d). Model output for the carbonate recrystallization + authigenic clay precipitation scenario, in which all model

parameters are the same as the simulations above ($K_{Li}=3\cdot10^{-3}$), except that the pore fluid δ^7Li values and pore fluid Li concentrations as functions of depth and time are constrained as described in the text. The (g) δ^7Li (‰) and (h) bulk carbonate Li concentration (μmol/kg) output for the scenario shown is one in which the pore fluid Li (i) concentration and (j) isotopic composition varies over time within (k) a 25-m reactive layer that is deposited at 125 m above basement. In all simulations, the initial pore fluid and bulk carbonate δ^7Li is assumed to be that inferred for seawater by Misra and Froelich (2012) over the depositional time scale appropriate to Site 1338. The bulk carbonate recrystallization rate (R) utilized in all the models shown in this figure is a function of sediment age (e.g., Fantle and DePaolo, 2006) and is constrained by our modeling of Sr geochemistry at Site 1338 ($R[Ma^{-1}] = 0.07 \cdot e^{-age/5.25}$; Fig. S3).

Consequently, we can qualitatively explain bulk carbonate δ^7Li at Site U1338 if we assume that initial bulk carbonate Li concentrations are generally relatively low, and that carbonate recrystallization operates in the presence of clay authigenesis. Clay authigenesis controls pore fluid δ^7Li, and establishes the isotopic leverage to alter carbonate during recrystallization at depth in the sedimentary column. Near the seawater-sediment interface, however, the decrease in δ^7Li relative to the global seawater curve reflects isotopic equilibration of the solid with pore fluid with a seawater-like δ^7Li ($\alpha_{carbonate-fluid} = 0.9955$). The increase lower in the section then reflects re-equilibration with a fractionated pore fluid (δ^7Li ~ 55‰). Further, because explaining relatively high bulk carbonate Li concentrations in the uppermost part of the section is difficult without invoking some temporal variability in the bulk solid (which we deem unlikely over the inferred time scales), we hypothesize that a greater proportion of foraminiferal tests with higher Li concentrations in the upper ~100 meters of the section accounts for the higher Li concentrations in the upper ~75 meters of the section.

There are two possibilities regarding the location of the high pore fluid δ^7Li in the sedimentary section, which we designate the 'reactive zone' (Fig. 10k): (1) that it always occurs at depth in the section, or (2) that it moves from the seawater-sediment interface to depth over

847 time. If we assume that the reactive zone is always relatively deep in the column, then
848 recrystallization does not explain the observations at the detailed level, and the modeled solid
849 looks similar to the recrystallization-only scenarios (Fig. 10a-f). Specifically, the diagenetic shift
850 in δ^7Li is negligible (Fig. S4) because the carbonate does not recrystallize significantly in the
851 lower part of the section.

852 Thus, there are two ways to explain our observations: (1) the reactive zone has shifted its
853 location over time or (2) the pore fluid over the past ~17.5 Ma has been significantly more
854 distilled than it is today. We explore the first hypothesis, as the second is limited by the
855 likelihood that pore fluid Li concentrations are >1 μM (which limits the distillation effect; note
856 that the distillation effect is impacted by changes in the reaction rate relative to the diffusive flux
857 and/or the initial pore fluid Li concentration). In the model, we do not model clay authigenesis
858 explicitly, but crudely approximate its effect on both pore fluid Li concentrations and δ^7Li by
859 assigning a reactive zone in which Li concentrations and isotopic compositions can be
860 maintained at values that are constant or vary over time (Fig. 10i-j). Because of the limited
861 functionality with regard to simulating clay authigenesis, the resulting simulations are meant
862 only to ascertain if recrystallization in the presence of clay authigenesis can explain the observed
863 carbonate δ^7Li trend and what that would require.

864 Based on our modeling efforts (Fig. 10g-h), we can explain the δ^7Li of the carbonate
865 fraction at Site U1338 by assuming that the reactive zone has migrated from the seawater-
866 sediment interface to its current depth over the past ~10-11 Ma. This is consistent with the
867 concept that clay authigenesis is promoted by biogenic silica, and that this process is not
868 necessarily constant in time. Interestingly, carbonate δ^7Li records the movement of the reactive

zone, which suggests bulk nannofossil ooze δ^7Li as a recorder of clay authigenesis in the sedimentary column.

It is also possible that the Li isotopic composition of carbonates is impacted by siliciclastic contamination, which is especially problematic in cases in which the mass balance favors the contaminating phase. We suggest that that the study of You et al. (2003), who analyzed bulk carbonate and pore fluids at Site 851, is an example of the impact of clay contamination on bulk nannofossil ooze δ^7Li. While Sites 851 and U1338 have similar lithologies and pore fluid Li concentration and δ^7Li depth profiles, bulk carbonate δ^7Li values at Site U1338 are quite different from those at Site 851 (Fig. 11a).

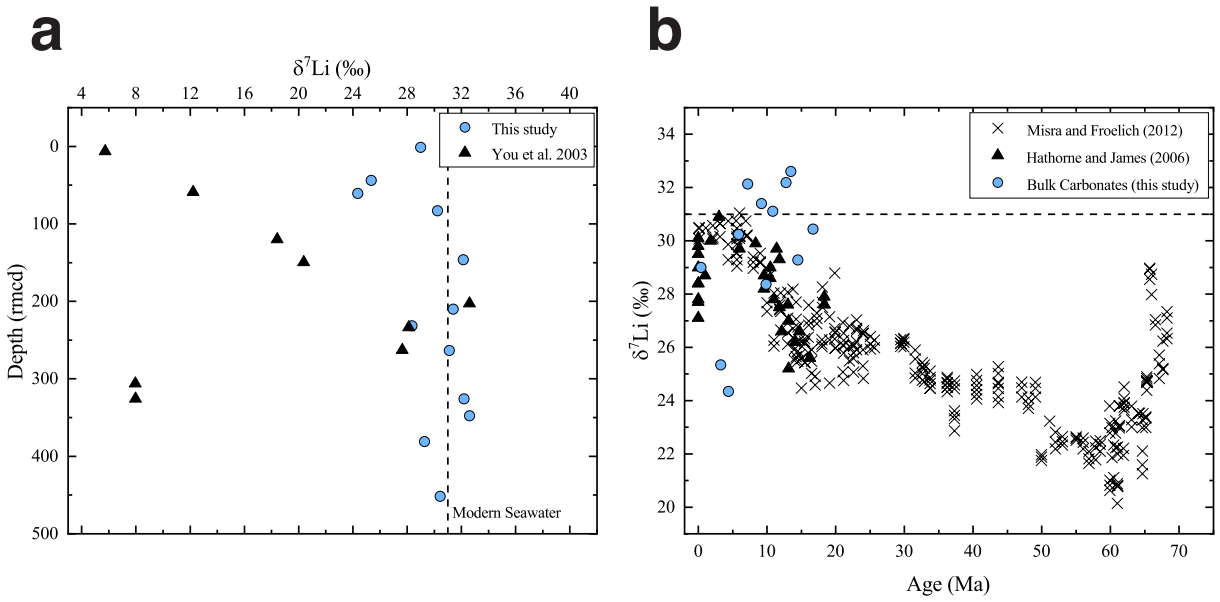

Figure 11. (a) Bulk carbonate isotopic composition of samples from Site U1338A plotted with bulk carbonate isotopic composition of samples from Site 851B (You et al., 2003). (b) Bulk carbonate isotopic composition of samples from Site U1338A plotted as a function of age alongside foraminiferal δ^7Li measured over the past 70 Ma (Misra and Froelich, 2012; James and Hathorne, 2006).

885 Various lines of evidence support our interpretation that bulk carbonate measurements at
886 Site 851 are impacted by clay contamination. First, bulk carbonates at Site U1338 are
887 isotopically similar to modern seawater, which is the expectation for marine carbonates (Hall et
888 al., 2005; Vigier et al., 2007). By contrast, the bulk carbonates from Site 851 have exceedingly
889 low δ^7Li values, in the range of the residual silicates at Site U1338 (Fig. 3). Second, the
890 interpretation put forth by You et al. (2003) was that the bulk carbonate δ^7Li depth profile was a
891 result of carbonate recrystallization. In this case, recrystallization would have to be close to
892 100% at ~250 meters, which is an extent of recrystallization not seen in modern nannofossil
893 oozes (Fantle and DePaolo, 2006; Fantle and DePaolo, 2007; Fantle et al., 2010; Fantle, 2015).
894 And finally, recent work has demonstrated that small quantities of clay have sufficient leverage
895 to alter the δ^7Li of bulk carbonates (Pogge von Strandmann et al., 2013).

896 Our data suggest that our measurements of δ^7Li are not impacted by clay contamination,
897 as the measured carbonate Li concentrations are quite low. Further, comparisons of our
898 carbonate δ^7Li to previously measured foraminiferal δ^7Li, especially in Unit III, support the
899 interpretation that bulk carbonate δ^7Li at Site U1338 reflects the impact of a post-depositional
900 process (Fig. 11b; Hathorne and James, 2006; Misra and Froelich, 2012). Thus, we conclude that
901 carbonate recrystallization in the presence of clay authigenesis explains the bulk carbonate data
902 at Site U1338.

903

904 **6 Conclusions**

905 The Li isotopic composition (δ^7Li) of pore fluids sampled from a carbonate-rich site
906 (IODP Site U1338) are presented and interpreted to reflect clay authigenesis in the sedimentary

column. Clay authigenesis sequesters Li in secondary clays, lowering pore fluid Li concentrations and generating Li concentration profiles that decrease strongly with depth and δ^7Li values that increase strongly with depth. Reactive transport models suggest that clay authigenesis, and not carbonate recrystallization, controls pore fluid δ^7Li; at a finer scale, the δ^7Li depth profile is best explained by an increase in reactivity (i.e., clay precipitation rate) at depth, and not changes in the isotopic fractionation factor associated with clay precipitation. Elucidating the control on the Li isotopic composition of marine pore fluids is important, as this signal can impact the δ^7Li of both siliciclastic proxy archives and carbonate proxy archives (i.e., via authigenesis, recrystallization, and/or contamination by siliciclastics).

We interpret the δ^7Li of chemically-cleaned carbonate at Site U1338 to be a consequence of recrystallization, but only in the presence of an active zone of clay authigenesis in the sedimentary column; recrystallization alone cannot explain carbonate δ^7Li, which is consistent with our interpretation of pore fluid δ^7Li. Using numerical models of carbonate recrystallization, we hypothesize that the reactive zone of clay authigenesis has moved from the surface to its current location over the past 10-11 Ma. This model-constrained conclusion provides support for the hypothesis that the isotopic composition of the authigenic clay sink for Li has varied over time.

The observations above are important because they highlight the role that clay authigenesis, particularly in carbonate-rich sections, could play in the global Li cycle. Assuming that clay authigenesis occurs to some extent in all carbonate-rich sections, we estimate that the output flux of Li into carbonate-rich sediments could reasonably be as large as $\sim 1.2 \cdot 10^{10}$ moles Li per year, which is similar to previous estimates of the mass flux required to balance the

929 modern Li budget. In theory, then, clay authigenesis in carbonate-rich sections may be a
930 significant contributor to the global Li cycle.

931 Moreover, it is often assumed that the Li isotopic composition of the authigenic sink is
932 simply related to the isotopic composition of seawater, modified by a fractionation factor (e.g.,
933 Misra and Froelich, 2012). However, this is only true when the reaction occurs at the seawater-
934 sediment interface. When the reaction occurs at depth, the pore fluid undergoes isotopic
935 distillation, which has two significant effects: (1) it reduces the leverage of clay authigenesis to
936 change seawater δ^7Li, and (2) the movement of the reactive zone relative to the seawater-
937 sediment interface drives secular variability in the δ^7Li of the output flux. Consequently, this
938 process, which is impacted by the reactivity of biogenic silica (or, in coastal sections,
939 continentally-derived silicate) and the relative rates of burial, transport, and reaction, can drive
940 long-term (i.e., on time scales of ~3-30 Ma, depending on the mass flux that one assumes)
941 changes in the δ^7Li of seawater. Ultimately, then, this flux must also be considered in
942 interpretations of proxy records, including the seawater δ^7Li record over the Cenozoic.

943

944 **7 Acknowledgements**

945 We would like to thank Ed Hathorne for providing squeeze-cake samples, and Jared Carte and
946 Matthew Gonzales for laboratory assistance. This manuscript was greatly improved by the
947 comments of two anonymous reviewers and AE James. Funding for this work was provided by
948 the National Science Foundation grant number 1446271 to MSF. PPvS and analyses at LOGIC
949 were funded by ERC Consolidator grant 682760 CONTROLPASTCO2.

References

Apitz S. E. (1991) The Lithification of Ridge Flank Basal Carbonates: Characterization and Implications for Sr/Ca and Mg/Ca in Marine Chalks and Limestones. University of California, San Diego.

Berner R. (1980) *Early Diagenesis A Theoretical Approach*., Princeton University Press, Princeton.

Burton K. W. and Vigier N. (2012) Lithium Isotopes as Tracers in Marine and Terrestrial Environments. In *Handbook of Environmental Isotope Geochemistry: Vol I* (ed. M. Baskaran). Springer Berlin Heidelberg, Berlin, Heidelberg. pp. 41–59.

Chan L.-H., Leeman W. P. and Plank T. (2006) Lithium isotopic composition of marine sediments. *Geochemistry, Geophys. Geosystems* **7**.

Chan L. H., Alt J. C. and Teagle D. A. H. (2002) Lithium and lithium isotope profiles through the upper oceanic crust: A study of seawater-basalt exchange at ODP Sites 504B and 896A. *Earth Planet. Sci. Lett.* **201**, 187–201.

Chan L. H., Edmond J. M., Thompson G. and Gillis K. (1992) Lithium isotopic composition of submarine basalts: implications for the lithium cycle in the oceans. *Earth Planet. Sci. Lett.* **108**, 151–160.

Chan L. H. and Kastner M. (2000) Lithium isotopic compositions of pore fluids and sediments in the Costa Rica subduction zone: Implications for fluid processes and sediment contribution to the arc volcanoes. *Earth Planet. Sci. Lett.* **183**, 275–290.

Chanda P. and Fantle M. S. (2017) Quantifying the effect of diagenetic recrystallization on the Mg isotopic composition of marine carbonates. *Geochim. Cosmochim. Acta* **204**, 219–239.

Chipera S. J. and Bish D. L. (2001) Baseline studies of the clay minerals society source clays: powder x-ray diffraction analyses. *Clays Clay Miner.* **49**, 398–409.

Delaney M. L. and Linn L. J. (1993) 33 . Interstitial Water and Bulk Calcite Chemistry, Leg 130, and Calcite Recrystalization. *Proc. Ocean Drill. Progr.* **130**, 561–572.

Dellinger M., Bouchez J., Gaillardet J., Faure L. and Moureau J. (2017) Tracing weathering regimes using the lithium isotope composition of detrital sediments. *Geology* **45**, 411–414.

Dellinger M., Gaillardet J., Bouchez J., Calmels D., Galy V., Hilton R. G., Louvat P. and France-Lanord C. (2014) Lithium isotopes in large rivers reveal the cannibalistic nature of modern continental weathering and erosion. *Earth Planet. Sci. Lett.* **401**, 359–372.

Dellinger M., Hardisty D. S., Planavsky N. J., Gill B. C., Kalderon-Asael B., Asael D., Croissant T., Swart P. K. and West A. J. (2020) The effects of diagenesis on lithium isotope ratios of shallow marine carbonates. *Am. J. Sci.* **320**, 150–184.

Dellinger M., Joshua West A., Paris G., Adkins J. F., Pogge von Strandmann P., Ullmann C. V., Eagle R. A., Freitas P., Bagard M.-L., Ries J. B., Corsetti F. A., Perez-Huerta A. and Kampf A. R. (2018) The Li isotope composition of marine biogenic carbonates: Patterns and Mechanisms. *Geochim. Cosmochim. Acta* **236**, 315–335.

Druhan J. L. and Maher K. (2014) A Model Linking Stable Isotope Fractionation to Water Flux and Transit Times in Heterogeneous Porous Media. *Procedia Earth Planet. Sci.* **10**, 179–188.

Fantle M. S. (2015) Calcium isotopic evidence for rapid recrystallization of bulk marine carbonates and implications for geochemical proxies. *Geochim. Cosmochim. Acta* **148**, 378–401.

Fantle M. S., Barnes B. D. and Lau K. V. (2020) The Role of Diagenesis in Shaping the Geochemistry of the Marine Carbonate Record. *Annu. Rev. Earth Planet. Sci.* **48**, 549–583.

Fantle M. S. and DePaolo D. J. (2007) Ca isotopes in carbonate sediment and pore fluid from ODP Site 807A: The Ca2+(aq)-calcite equilibrium fractionation factor and calcite recrystallization rates in Pleistocene sediments. *Geochim. Cosmochim. Acta* **71**, 2524–2546.

Fantle M. S. and DePaolo D. J. (2006) Sr isotopes and pore fluid chemistry in carbonate sediment of the Ontong Java Plateau: Calcite recrystallization rates and evidence for a rapid rise in seawater Mg over the last 10 million years. *Geochim. Cosmochim. Acta* **70**, 3883–3904.

Fantle M. S. and Higgins J. (2014) The effects of diagenesis and dolomitization on Ca and Mg isotopes in marine platform carbonates: Implications for the geochemical cycles of Ca and Mg. *Geochim. Cosmochim. Acta* **142**, 458–481.

Fantle M. S., Maher K. M. and DePaolo D. J. (2010) Isotopic approaches for quantifying the rates of marine burial diagenesis. *Rev. Geophys.* **48**, 1–38.

Fernandez N. M., Zhang X. and Druhan J. L. (2019) Silicon isotopic re-equilibration during amorphous silica precipitation and implications for isotopic signatures in geochemical proxies. *Geochim. Cosmochim. Acta* **262**, 104–127.

Geilert S., Vroon P. Z., Roerdink D. L., Van Cappellen P. and van Bergen M. J. (2014) Silicon isotope fractionation during abiotic silica precipitation at low temperatures: Inferences from flow-through experiments. *Geochim. Cosmochim. Acta* **142**, 95–114.

Gorski C. A. and Fantle M. S. (2017) Stable mineral recrystallization in low temperature aqueous systems: A critical review. *Geochim. Cosmochim. Acta* **198**, 439–465.

Hall J. M., Chan L. H., McDonough W. F. and Turekian K. K. (2005) Determination of the lithium isotopic composition of planktic foraminifera and its application as a paleo-seawater proxy. *Mar. Geol.* **217**, 255–265.

Hathorne E. C. and James R. H. (2006) Temporal record of lithium in seawater: A tracer for silicate weathering? *Earth Planet. Sci. Lett.* **246**, 393–406.

Hein J. R., Yeh H. W. and Alexander E. (1979) Origin of iron-rich montmorillonite from the manganese nodule belt of the North Equatorial Pacific. *Clays Clay Miner.* **27**, 185–194.

Hindshaw R. S., Tosca R., Goût T. L., Farnan I., Tosca N. J. and Tipper E. T. (2019) Experimental constraints on Li isotope fractionation during clay formation. *Geochim. Cosmochim. Acta* **250**, 219–237.

Hoefs J. and Sywall M. (1997) Lithium isotope composition of Quaternary and Tertiary biogene carbonates and a global lithium isotope balance. *Geochim. Cosmochim. Acta* **61**, 2679–2690.

Huber C., Druhan J. L. and Fantle M. S. (2017) Perspectives on geochemical proxies: The impact of model and parameter selection on the quantification of carbonate recrystallization rates. *Geochim. Cosmochim. Acta* **217**, 171–192.

Huh Y., Chan L. H., Zhang L. and Edmond J. M. (1998) Lithium and its isotopes in major world rivers: implications for weathering and the oceanic budget. *Geochim. Cosmochim. Acta* **62**, 2039–2051.

Kisakurek B., James R. H. and Harris N. B. W. (2005) Li and δ7Li in Himalayan rivers: Proxies for silicate weathering? *Earth Planet. Sci. Lett.* **237**, 387–401.

Lechler M., Pogge von Strandmann P. A. E., Jenkyns H. C., Prosser G. and Parente M. (2015) Lithium-isotope evidence for enhanced silicate weathering during OAE 1a (Early Aptian Selli event). *Earth Planet. Sci. Lett.* **432**, 210–222.

Li G. and West A. J. (2014) Evolution of Cenozoic seawater lithium isotopes: Coupling of global denudation regime and shifting seawater sinks. *Earth Planet. Sci. Lett.* **401**, 284–293.

Magna T., Wiechert U. H. and Halliday A. N. (2004) Low-blank isotope ratio measurement of small samples of lithium using multiple-collector ICPMS. *Int. J. Mass Spectrom.* **239**, 67–76.

Marriott C. S., Henderson G. M., Belshaw N. S. and Tudhope A. W. (2004a) Temperature dependence of δ7Li, δ44Ca and Li/Ca during growth of calcium carbonate. *Earth Planet. Sci. Lett.* **222**, 615–624.

Marriott C. S., Henderson G. M., Crompton R., Staubwasser M. and Shaw S. (2004b) Effect of mineralogy, salinity, and temperature on Li/Ca and Li isotope composition of calcium carbonate. *Chem. Geol.* **212**, 5–15.

Martin J. B., Kastner M. and Elderfield H. (1991) Lithium: sources in pore fluids of Peru slope sediments and implications for oceanic fluxes. *Mar. Geol.* **102**, 281–292.

Michalopoulos P. and Aller R. (1995) Rapid Clay Mineral Formation in Amazon Delta Sediments: Reverse Weathering and Oceanic Elemental Cycles. *Science (80-.).* **270**, 614–617.

Michalopoulos P. and Aller R. C. (2004) Early diagenesis of biogenic silica in the Amazon delta: Alteration, authigenic clay formation, and storage. *Geochim. Cosmochim. Acta* **68**, 1061–1085.

Michalopoulos P., Aller R. C. and Reeder R. J. (2000) Conversion of diatoms to clays during early diagenesis in tropical, continental shell muds. *Geology* **28**, 1095–1098.

Millot R., Vigier N. and Gaillardet J. (2010) Behaviour of lithium and its isotopes during weathering in the Mackenzie Basin, Canada. *Geochim. Cosmochim. Acta* **74**, 3897–3912.

Misra S. and Froelich P. N. (2012) Lithium Isotope History of Cenozoic Seawater: Changes in

Silicate Weathering and Reverse Weathering. *Science (80-.).* **335**, 818–823.

Palïke H., Lyle M., Raffi I. and Klaus A. (2010a) Methods. *Proc. IODP* **320**.

Palïke H., Lyle M., Raffi I. and Klaus A. (2010b) Site U1338 Report. *Proc. IODP* **320**.

Pistiner J. S. and Henderson G. M. (2003) Lithium-isotope fractionation during continental weathering processes. *Earth Planet. Sci. Lett.* **214**, 327–339.

Pogge von Strandmann P. A. ., Desrochers A., Murphy M. J., Finlay A. J., Selby D. and Lenton T. M. (2017) Global climate stabilisation by chemical weathering during the Hirnantian glaciation. *Geochemical Perspect. Lett.* **3**, 230–237.

Pogge von Strandmann P. A. E., Elliott T., Marschall H. R., Coath C., Lai Y.-J., Jeffcoate A. B. and Ionov D. A. (2011) Variations of Li and Mg isotope ratios in bulk chondrites and mantle xenoliths. *Geochim. Cosmochim. Acta* **75**, 5247–5268.

Pogge von Strandmann P. A. E., Fraser W. T., Hammond S. J., Tarbuck G., Wood I. G., Oelkers E. H. and Murphy M. J. (2019a) Experimental determination of Li isotope behaviour during basalt weathering. *Chem. Geol.* **517**, 34–43.

Pogge von Strandmann P. A. E., James R. H., van Calsteren P., Gíslason S. R. and Burton K. W. (2008) Lithium, magnesium and uranium isotope behaviour in the estuarine environment of basaltic islands. *Earth Planet. Sci. Lett.* **274**, 462–471.

Pogge von Strandmann P. A. E., Jenkyns H. C. and Woodfine R. G. (2013) Lithium isotope evidence for enhanced weathering during Oceanic Anoxic Event 2. *Nat. Geosci.* **6**, 668–672.

Pogge von Strandmann P. A. E., Schmidt D. N., Planavsky N. J., Wei G., Todd C. L. and Baumann K. H. (2019b) Assessing bulk carbonates as archives for seawater Li isotope ratios. *Chem. Geol.* **530**, 119338.

Richter F. M. and DePaolo D. J. (1987) Numerical models for diagenesis and the Neogene Sr isotopic evolution of seawater from DSDP Site 590B. *Earth Planet. Sci. Lett.* **83**, 27–38.

Richter F. M., Mendybaev R. a., Christensen J. N., Hutcheon I. D., Williams R. W., Sturchio N. C. and Beloso A. D. (2006) Kinetic isotopic fractionation during diffusion of ionic species in water. *Geochim. Cosmochim. Acta* **70**, 277–289.

Roerdink D. L., van den Boorn S. H. J. M., Geilert S., Vroon P. Z. and van Bergen M. J. (2015) Experimental constraints on kinetic and equilibrium silicon isotope fractionation during the formation of non-biogenic chert deposits. *Chem. Geol.* **402**, 40–51.

Rudnick R. L., Tomascak P. B., Njo H. B. and Gardner L. R. (2004) Extreme lithium isotopic fractionation during continental weathering revealed in saprolites from South Carolina. *Chem. Geol.* **212**, 45–57.

Schrag D. P., DePaolo D. J. and Richter F. M. (1992) Oxygen Isotope Exchange in a 2-Layer Model of Oceanic-Crust. *Earth Planet. Sci. Lett.* **111**, 305–317.

Spinelli G. A., Giambolvo E. R. and Fisher A. T. (2004) Sediment permeability, distribution, and influence on fluxes in oceanic basement. In *Hydrogeology of the Oceanic Lithosphere* (eds.

E. E. Davis and H. Elderfield). Cambridge University Press. pp. 151–188.

Steefel C. I., Appelo C. A. J., Arora B., Jacques D., Kalbacher T., Kolditz O., Lagneau V., Lichtner P. C., Mayer K. U., Meeussen J. C. L., Molins S., Moulton D., Shao H., Šimůnek J., Spycher N., Yabusaki S. B. and Yeh G. T. (2015) *Reactive transport codes for subsurface environmental simulation*.,

Steefel C. I., Druhan J. L. and Maher K. (2014) Modeling Coupled Chemical and Isotopic Equilibration Rates. *Procedia Earth Planet. Sci.* **10**, 208–217.

Stoffyn-Egli P. and Mackenzie F. T. (1984) Mass balance of dissolved lithium in the oceans. *Geochim. Cosmochim. Acta* **48**, 859–872.

Tomascak P. B., Magna T. and Dohmen R. (2016) *Advances in Lithium Isotope Geochemistry*., Springer.

Turcotte D. L. and Schubert G. (1982) *Geodynamics applications of continuum physics to geological problems*., John Wiley and Sons, Inc., New York.

Ullmann C. V, Campbell H. J., Frei R., Hesselbo S. P., Pogge von Strandmann P. A. E. and Korte C. (2013) Partial diagenetic overprint of Late Jurassic belemnites from New Zealand: Implications for the preservation potential of δ7Li values in calcite fossils. *Geochim. Cosmochim. Acta* **120**, 80–96.

Verney-Carron A., Vigier N. and Millot R. (2011) Experimental determination of the role of diffusion on Li isotope fractionation during basaltic glass weathering. *Geochim. Cosmochim. Acta* **75**, 3452–3468.

Vigier N., Decarreau A., Millot R., Carignan J., Petit S. and France-Lanord C. (2008) Quantifying Li isotope fractionation during smectite formation and implications for the Li cycle. *Geochim. Cosmochim. Acta* **72**, 780–792.

Vigier N., Rollion-Bard C., Spezzaferri S. and Brunet F. (2007) In situ measurements of Li isotopes in foraminifera. *Geochemistry, Geophys. Geosystems* **8**.

Voigt J., Hathorne E. C., Frank M., Vollstaedt H. and Eisenhauer A. (2015) Variability of carbonate diagenesis in equatorial Pacific sediments deduced from radiogenic and stable Sr isotopes. *Geochim. Cosmochim. Acta* **148**, 360–377.

Wimpenny J., Colla C. A., Yu P., Yin Q. Z., Rustad J. R. and Casey W. H. (2015) Lithium isotope fractionation during uptake by gibbsite. *Geochim. Cosmochim. Acta* **168**, 133–150.

You C. F., Chan L. H., Gieskes J. M. and Klinkhammer G. P. (2003) Seawater intrusion through the oceanic crust and carbonate sediment in the Equatorial Pacific: Lithium abundance and isotopic evidence. *Geophys. Res. Lett.* **30**, 2120.

You C. F., Chan L. H., Spivack A. J. and Gieskes J. M. (1995) Lithium, boron, and their isotopes in sediments and pore waters of Ocean Drilling Program site 808, Nankai Trough: implications for fluid expulsion in accretionary prisms. *Geology* **23**, 37–40.

Zhang L., Chan L. H. and Gieskes J. M. (1998) Lithium isotope geochemistry of pore waters from Ocean Drilling Program Sites 918/919, Irminger Basin. *Geochim. Cosmochim. Acta*

62, 2437–2450.